

EXPERIMENTAL CHARACTERIZATION OF PROPELLER-WING INTERACTIONS FOR A SUBSCALE LIFT + CRUISE VTOL UAV

Pratibha Bhandari[1], Zach Atkinson[1] & Anthony Comer[1]

[1]School of Mechanical and Aerospace Engineering, Oklahoma State University , Tulsa, OK, USA

Abstract

This paper experimentally characterizes lift-propeller-wing aerodynamic interactions for a subscale lift-plus-cruise vertical takeoff and landing unmanned aerial vehicle during transition-representative conditions. The S2F-X200 test vehicle is used as the reference configuration, with emphasis on the effect of fore lift-propeller wake impingement on downstream wing loading and control-surface effectiveness. Experiments are conducted in WindShape® fan-array facilities using isolated propeller, propeller-wing baseline, and propeller-wing active configurations mounted to an ATI Delta six-axis force and moment balance. The test matrix varies freestream velocity, propeller rotational speed, propeller placement, and control-surface deflection. The measured results show that fore lift-propeller operation produces measurable changes in wing force and pitching-moment response relative to the baseline case, with the strongest differences appearing in the control surface pitching moment increments. Comparisons with a non-interacting blade-element and strip-theory simulation model show that these effects are not captured by clean wing or uncoupled propeller models. The results provide experimental evidence of lift-propeller-wing coupling in lift-plus-cruise aircraft and support future reduced-order modeling for flight simulation and control-law design.

Keywords: Propeller-Wing Interactions, VTOL, Transition Flight, Experimental Validation, Reduced-Order Modeling

1. Introduction

Vertical take-off and landing (VTOL) configurations, including lift + cruise (LPC) designs that employ dedicated lift propellers for: (i) hover, (ii) low-speed operations, and (iii) transition to and from forward flight, face notable aero-propulsive interactions during transition. As the aircraft accelerates, the incoming flow produces a skewed inflow with axial and tangential wake components, altering the local flow over the wings and control surfaces. Understanding propeller-wing interactions in these regimes is therefore essential for safe and efficient operation.

Prior studies on rotor-wing aerodynamic interactions have largely focused on wing-blown [1] [2] [3] [4] or tilt-rotor configurations, with limited attention to lift + cruise (LPC) architectures, wherein dedicated lift propellers affect lifting surface and control surface performance in transition. Lim performed a computational study of proprotor–wing aerodynamic interactions for a tilt-rotor in airplane (forward flight) mode, identifying thrust and drag variations due to rotor-wing interference [5]. Srivathsan and Rauleder experimentally examined propeller–wing interaction under a zero-tilt, forward flight condition [6]. Both studies focus on cruise configurations and do not address the aerodynamic interactions specific to LPC transitional modes. Similarly, studies have been conducted extensively to experimentally examine the influence of rotor and rotor–wing geometry on wing aerodynamic loading [7], and to analytically investigate rotor–wing interactional aerodynamics and inflow behavior [8] in hover for the V-22 tilt-rotor configuration, where wake skew effects are minimal.

DOI: https://doi.org/10.71945/icas2026_0689

Recent studies have investigated the wing-propeller interaction on rear propellers in LPC configurations during transition. These investigations show that aerodynamic coupling occurs in both directions: wing-induced downwash modifies the inflow experienced by the rear propellers, influencing required thrust, power consumption, and dynamic stability characteristics [9], while rear propeller wake impingement alters the wing pressure distribution, producing jet-flap-like lift augmentation or adverse pressure gradients depending on axial and longitudinal separation [10]. Together, these works demonstrate that rear wing–propeller interaction plays a critical role in transition performance, trim behavior, and stability of lift-plus-cruise aircraft. However, experimental data are still needed to quantify the effect of fore lift-propeller wakes on downstream lifting surfaces and control surfaces in lift-plus-cruise configurations during transition.

This study investigates lift-propeller downwash effects on downstream wing aerodynamics and control-surface effectiveness in a LPC configuration during transition flight. To achieve this, ATI Delta six-axis force-balance measurements are acquired in WindShape®-generated flow fields for a representative S2F-X200 wing-boom-propeller assembly. The experiments examine variations in longitudinal and vertical fore-propeller placement, control-surface deflection, and representative transition trim conditions. Isolated propeller, propeller-wing baseline, and propeller-wing active configurations are used to separate clean-wing behavior, isolated propeller loading, and propeller-induced changes in the downstream wing response. A non-interacting blade-element and strip-theory simulation model is used as a baseline for comparison, allowing experimentally observed differences to be interpreted as propeller-wing interaction effects not captured by uncoupled aerodynamic and propulsive models. Through this framework, the study provides experimental evidence of lift-propeller-wing coupling during transition and establishes a data foundation for future reduced-order interaction modeling.



Figure 1 – S2F-X200 LPC VTOL configuration with former 3-bladed propellers

1.1 Aircraft Configuration Overview

This work uses the S2F-X200 LPC VTOL configuration (Fig.1) as the test vehicle, designed and built at the Simulation to Flight Applied Research Laboratory at Oklahoma State University (OSU). The S2F-X200 is a fixed, high-mounted wing LPC configuration with a conventional empennage. The wing includes two inboard flaperons and two outboard ailerons. The empennage consists of a horizontal stabilizer with two elevators and a vertical stabilizer with a rudder. The vehicle characteristics are outlined further in Table 1. The propulsion system consists of four (4) Cobra CM4510 420 KV motors for the lift propulsors and one (1) Cobra C-4120/18 brushless 540 KV motor for forward flight. The system is equipped with four lift propellers mounted on lateral booms and a single fuselage mounted pusher (cruise) propeller for forward thrust. The lift motors are equipped with APC 16x5.5 MR propellers, while the cruise propeller is an APC 16×10E model. All propulsors and aerodynamic surfaces are fixed in orientation, with no tilt or vectoring mechanisms employed during VTOL or forward flight. During vertical flight, lift generation and attitude control (roll, pitch, and yaw) are achieved through the

four lift props, similar to a conventional quadcopter system. In forward flight, roll, pitch, and yaw are controlled using the ailerons, elevators, and rudder, respectively.

Table 1 – S2F-X200 vehicle parameters and mass properties.

Parameter	Metric units	English units
Maximum takeoff mass (MTOM)	10.4 kg	23.0 lbs
Empty takeoff mass (ETOM, w/o payload)	7.72 kg	17.0 lbs
Battery mass	1.30 kg	2.86 lbs
Payload mass	2.72 kg	6.00 lbs
Wing area	0.50 m^2	5.42 ft^2
Wing span	2.00 m	6.56 ft
Horizontal tail span	0.58 m	1.92 ft
Vertical tail span	0.20 m	0.67 ft
Fuselage length	1.47 m	4.81 ft
Lift propeller diameter	0.41 m	16 in
Lift propeller cant angle	$\pm 15^\circ$	$\pm 15^\circ$
Lift motor rated power (each)	4 $\times$ 1375 W	4 $\times$ 1.05 hp
Cruise propeller diameter	0.38 m	16.0 in
Cruise motor rated power	1200 W	1.61 hp
Wing loading (ETOM)	15.4 kg/m^2	3.16 lb/ft^2
Disc loading (ETOM, hover)	14.9 kg/m^2	3.05 lb/ft^2

2. Baseline Simulation Modeling Approach

The *Versatile Integrated Simulation and Testing Architecture* (VISTA) is a MATLAB/Simulink-based environment for flight dynamics simulation, control law design, and hardware-compatible implementation. Models are assembled from modular subsystems so that different vehicle configurations can be represented with a common structure while preserving the ability to exchange aerodynamic, propulsive, and control components as needed. For this study, VISTA is used to construct a non-interacting baseline simulation model of the experimental test article. The propulsors are represented using a blade element theory (BET) model with dynamic inflow, while the wing and lifting surfaces are modeled using strip-theory. The resulting simulation model is used to predict the isolated propeller response and the clean propeller-wing baseline response for each experimental test case. No propeller-wing interaction corrections are included in the baseline simulation model; therefore, differences between the modeled and measured propeller-wing active cases are interpreted as experimentally observed interaction effects.

2.1 Propeller Modeling Approach

Each lift propeller is modeled using a quasi-steady blade element theory (BET) framework combined with a seven-state Pitt–Peters dynamic inflow formulation [11]. The propellers are modeled as rigid, fixed-pitch rotors with RPM control; therefore, cyclic pitch, flapping, and lead-lag dynamics are not modeled in this study. The inflow model represents the time-dependent behavior of the induced velocity field through three primary inflow states and four additional wake distortion states. Specifically, the states correspond to the mean induced inflow (v_{i0}), first-harmonic sine and cosine inflow components (v_{1s}, v_{1c}), wake skew (χ), wake spacing (S), and longitudinal and lateral wake curvature (k_c, k_s).

The non-dimensional advance ratio and inflow are defined as $\mu = V_\infty/(\Omega R)$ and $\lambda = v_i/(\Omega R)$, respectively. The instantaneous skew angle of the rotor wake is computed as

$$\chi = \tan^{-1}\left(\frac{\mu}{\lambda + \mu_z}\right), \tag{1}$$

where μ_z denotes the non-dimensional climb velocity component. Quasi-steady approximations for the wake parameters follow from the Pitt–Peters and Zhao [11] dynamic wake distortion model, yield-

ing $\chi_{qs} = \tan(\chi/2)$, $S_{qs} = 2\pi V_m$, and curvature terms $k_{c,qs}$ and $k_{s,qs}$ expressed as functions of the instantaneous non-dimensional pitch and roll rates, respectively.
In the present study, the propeller model is used to predict isolated propeller forces and moments and to provide estimates of induced velocity and wake skew for interpreting the experimental trends. Propeller-wing interaction corrections are not applied to the downstream strip-theory aerodynamic model in the baseline simulation results. Therefore, the propeller and wing models remain uncoupled, and differences between the measured propeller-wing active cases and the non-interacting simulation predictions are used to identify interaction effects.
Interference between the propulsors and supporting booms is represented using a thrust-reduction factor based on boom geometry and propeller diameter [12, 13]. More detailed slipstream-shape and flow-acceleration models, such as super-Gaussian wake profiles [14] and propeller slipstream formulations based on McCormick [15], Stone [3], and Cook and Hauser [16], are retained as candidates for future coupled reduced-order modeling but are not used to modify wing-strip velocities in the baseline comparisons presented here.

2.2 Aerodynamic Modeling Approach

The aerodynamic model employed in this study follows a strip-theory formulation consistent with the methods presented in [17, 18, 19]. The wing is discretized into spanwise strips extending from root to tip, as shown in Fig. 2. Aerodynamic loads are evaluated at the aerodynamic center of each strip, taken at the quarter-chord location, using sectional airfoil coefficients obtained from XFOIL [20]. The sectional lift, drag, and pitching-moment coefficients, C_l, C_d, and C_{m_y}, are tabulated as functions of effective angle of attack and interpolated during simulation.

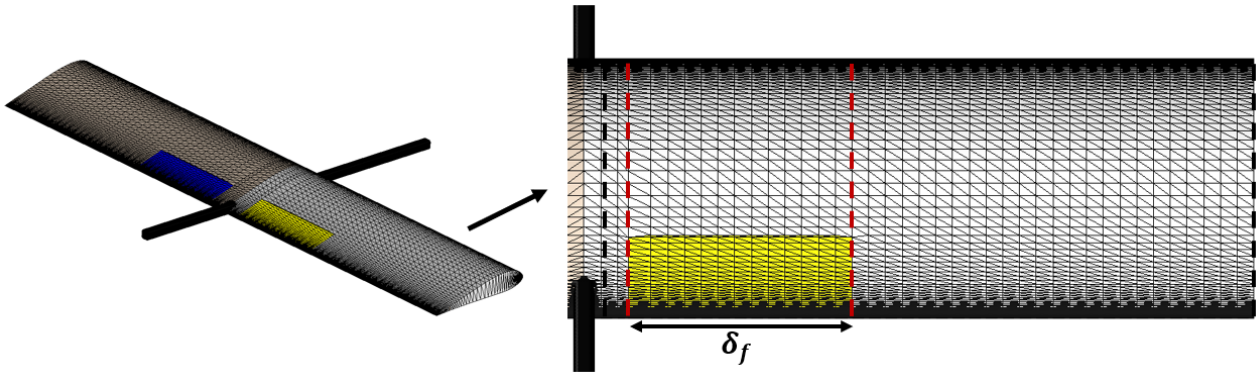


Figure 2 – Strip definition along the test-section wing, with the control-surface region highlighted.

Finite-wing circulation effects are incorporated using the FlightStream® ROM toolbox, which provides a precomputed downwash distribution across the lifting surfaces. This downwash model is used to define an induced angle of attack, $\alpha_{ind,i}$, for each strip. The local effective angle of attack is then computed as

$$\alpha_{eff,i} = \alpha_{\infty,i} - \alpha_{ind,i}, \tag{2}$$

where $\alpha_{\infty,i}$ is the local synthetic angle of attack, including geometric incidence and control-surface deflection effects.
For strips containing control surfaces, the local incidence is adjusted using an equivalent angle-of-attack increment,

$$\Delta\alpha_f = \tan^{-1}\left(\frac{\lambda \sin\delta}{1-\lambda+\lambda\cos\delta}\right), \qquad \lambda \in [0,1], \tag{3}$$

where λ is the fraction of the local chord occupied by the control surface and δ is the control surface deflection angle. The corresponding synthetic angle of attack is

$$\alpha_{\infty,i} = \alpha_{geom,i} + \Delta\alpha_f, \tag{4}$$

where $\alpha_{geom,i}$ is the geometric angle of attack of the strip. This control-surface representation is illustrated in Fig. 3.

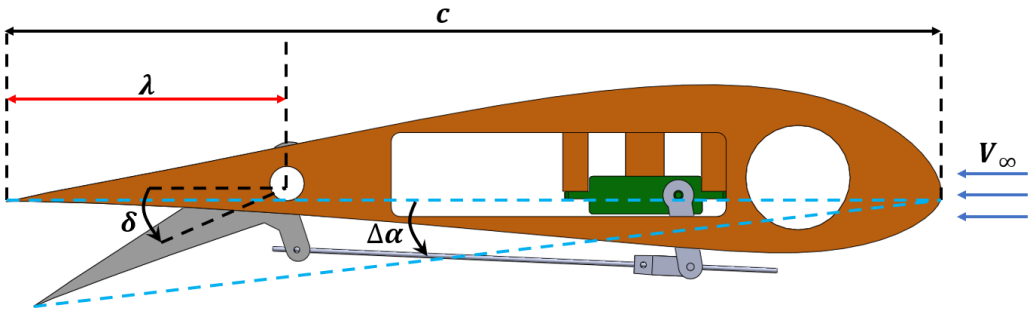


Figure 3 – Geometric representation of control-surface deflection as an equivalent angle-of-attack increment.

The interpolated sectional coefficients are converted into dimensional strip forces and moments according to

$$\begin{bmatrix} F_{x_s} \\ F_{y_s} \\ F_{z_s} \end{bmatrix} = -\bar{q}_i S_i \begin{bmatrix} \cos\alpha_{geom,i} & 0 & -\sin\alpha_{geom,i} \\ 0 & 1 & 0 \\ \sin\alpha_{geom,i} & 0 & \cos\alpha_{geom,i} \end{bmatrix} \begin{bmatrix} C_d \\ 0 \\ C_l \end{bmatrix}, \qquad \begin{bmatrix} M_{x_s} \\ M_{y_s} \\ M_{z_s} \end{bmatrix} = \bar{q}_i S_i \bar{c}_i \begin{bmatrix} 0 \\ C_{m_y} \\ 0 \end{bmatrix}. \tag{5}$$

Here, $\bar{q}_i$ is the local strip dynamic pressure, S_i is the strip planform area, and $\bar{c}_i$ is the local strip chord. The strip-level forces and moments are transformed into the load-cell coordinate system and summed to produce total predicted forces and moments for the clean propeller-wing baseline configuration.
In the present study, this aerodynamic model is used only for the non-interacting baseline comparisons. Propeller-induced changes in local velocity, dynamic pressure, or angle of attack are not applied to the wing strips in the baseline model. Therefore, differences between the measured propeller-wing active cases and the baseline model predictions are interpreted as propeller-wing interaction effects.

3. Experimental Setup

The experimental campaign was designed to characterize the effect of fore lift-propeller operation on the downstream wing and control surfaces of the S2F-X200 lift-plus-cruise configuration. Five primary test parameters were varied: boom distance, x_b; propeller height, h_r; freestream velocity, V_∞; propeller rotational speed, N; and control-surface deflection, δ. The boom distance, x_b, is defined as the chordwise position of the fore propeller relative to the wing quarter-chord location, while h_r is defined as the vertical offset between the propeller plane and the wing chord line. These parameters are illustrated in Fig. 3..

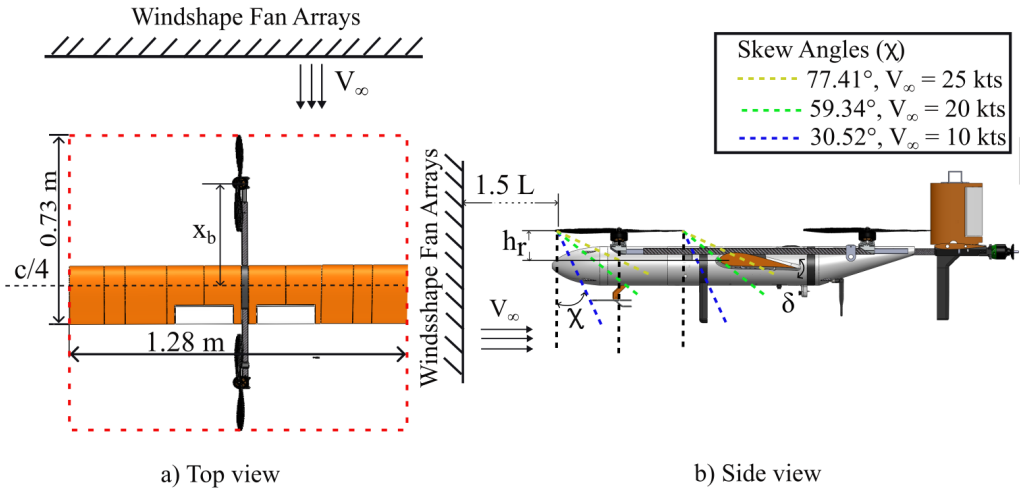


Figure 4 – Experimental test-section definition for the propeller-wing configuration, shown for $x_b = 2R$ and $h_r = 0.23R$; schematic not to scale.

Three experimental configurations were tested to separate the primary aerodynamic contributions. The first configuration was an isolated propeller case, in which a single lift propulsor was mounted directly to the ATI Delta six-axis force and moment balance and characterized independently. This configuration is hereafter referred to as the *Isolated Propeller* case and is used to establish the standalone force and moment response of the lift propulsor.
The second configuration was a propeller-wing baseline case, in which the wing-boom-propeller assembly was mounted to the force balance with the lift propellers installed but inactive. This configuration is hereafter referred to as the *Propeller-Wing Baseline* case and provides a reference measurement for the wing, boom, inactive propellers, and mounting hardware in the absence of propeller-induced flow.
The third configuration was a propeller-wing active case, in which the same wing–boom–propeller assembly was tested with the lift propellers operating. This configuration is hereafter referred to as the *Propeller-Wing Active* case. Comparisons between the *Propeller-Wing Baseline* and *Propeller-Wing Active* cases are used to quantify the aerodynamic increments associated with propeller operation. These increments include both the direct propeller loads transmitted through the test article and the interaction effects caused by propeller wake impingement on the downstream wing and control surfaces. The isolated propeller measurements provide a reference for interpreting the standalone contribution of the propulsor.

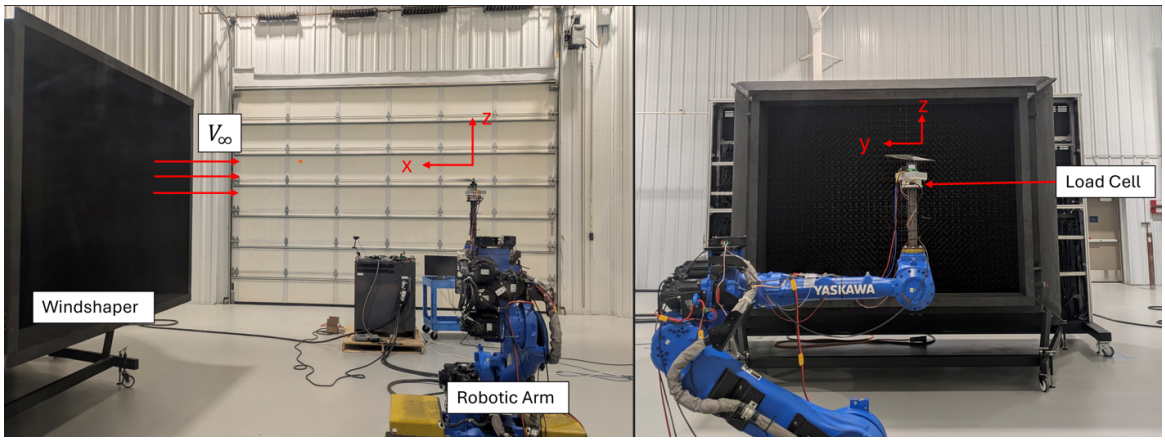


Figure 5 – Isolated propeller experiments conducted in the 3.2 m $\times$ 2.4 m WindShape® fan-array facility.

3.1 Isolated Propeller Characterization Experimental Setup

Isolated propeller experiments were conducted for the APC 16$\times$5.5 MR propeller using the WindShape® fan-array facility in Tulsa, Oklahoma. The experimental setup consisted of a 3.2 m $\times$ 2.4 m WindShape® fan array, a Yaskawa MH50 II robotic arm, an ATI Delta six-axis force and moment balance [21], and an S2F-X200 lift propulsor, as shown in Fig. 5. These tests were used to characterize the standalone propeller force and moment response as a function of freestream velocity and rotational speed.
The WindShaper system is a modular wind-generation platform composed of independently controlled fans that produce spatially uniform and repeatable flow conditions. For the isolated propeller tests, the fan array was equipped with a converging nozzle having a throat-area ratio of 2.7:1 relative to the fan-array area and a length of approximately 2.75 m. The nozzle increases the maximum flow speed to approximately 30 m/s at 100% fan power. Operation of the fan array, robotic arm, and force balance was coordinated through custom in-house data-acquisition software developed by WindShape®.
Force and moment measurements were acquired at 2000 Hz and included three-axis forces, F_x, F_y, and F_z, and three-axis moments, M_x, M_y, and M_z. The ATI Delta load-cell limits are summarized in Table 2, and the load-cell axis convention is shown in Fig. 6.
The lift propulsor consisted of a Cobra CM4510 420 KV motor driving an APC 16$\times$5.5 MR propeller, powered by a 100 A electronic speed controller and a 6S LiPo battery. The propulsor was mounted

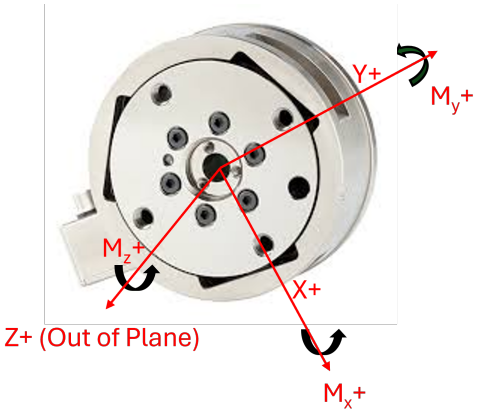


Figure 6 – ATI Delta load cell.

Table 2 – ATI Delta load cell axis limits.

Axis	Limit
F_x, F_y	660 N
F_z	1980 N
M_x, M_y	60 N·m
M_z	60 N·m
Measurement uncertainty	95%

along the load-cell z-axis, as illustrated in Fig. 5. The load-cell x-axis was oriented positive toward the WindShape® fan array.

Steady-state propulsor characterization was performed using a staircase input sequence. The electronic speed controller was commanded with discrete PWM inputs, with each command held for a fixed duration before increasing to the next value. This procedure allowed the propeller rotational speed to reach a steady value at each operating point. The PWM range was 1000 μs to 1700 μs, with increments of 50 μs and a hold time of 10 s at each command. The test sequence was performed under static conditions and repeated at freestream velocities of $V_\infty = [5, 10, 15, 20]$ m/s. Each condition was repeated three times to assess repeatability.

Propeller rotational speed was estimated from the measured force data using frequency-domain analysis. The blade-passing frequency, f_{BPF}, was identified from the measured response, and the corresponding rotational speed was computed as

$$\mathrm{RPM} = \frac{60\, f_{\mathrm{BPF}}}{N_b}, \tag{6}$$

where N_b is the number of propeller blades.

The measured forces and moments were non-dimensionalized using the propeller diameter and rotational speed according to Eqs. 7 and 8 [22, 23]:

$$C_{F_x} = \frac{F_x}{\rho n^2 d^4}, \qquad C_{F_y} = \frac{F_y}{\rho n^2 d^4}, \qquad C_{F_z}\,(C_T) = \frac{F_z}{\rho n^2 d^4}, \tag{7}$$

$$C_{M_x} = \frac{M_x}{\rho n^2 d^5}, \qquad C_{M_y} = \frac{M_y}{\rho n^2 d^5}, \qquad C_{M_z}\,(C_Q) = \frac{M_z}{\rho n^2 d^5}. \tag{8}$$

Here, ρ is the air density, d is the propeller diameter, and $n = \mathrm{RPM}/60$ is the rotational speed in revolutions per second. The thrust coefficient, C_T, is associated with the measured load-cell force component F_z, while the torque coefficient, C_Q, is associated with the measured load-cell moment component M_z.

3.2 Propeller-Wing Experimental Setup

The experimental setup for the *Propeller-Wing Baseline* and *Propeller-Wing Active* cases is shown in Fig. 7. The setup consisted of the forward and aft lift propulsors, together with the left wing-boom assembly section from the S2F-X200 aircraft. The S2F-X200 avionics system was used to control the operation of the wing-boom-propeller assembly. The apparatus was mounted on an ATI Delta six-axis force and moment balance, which was mounted on an in-house-manufactured aluminum-frame testing rig. The avionics components were placed at the bottom of the testing rig.

The experiments were conducted using the WindShape® fan arrays at OSU-Tulsa, with test sections measuring 7.9 ft $\times$ 6.3 ft (2.4 m x 1.9 m). The fan arrays produce a constant 16 m/s flow at 100% power. Figure 8 illustrates the experimental testing facility layout with a representative test article

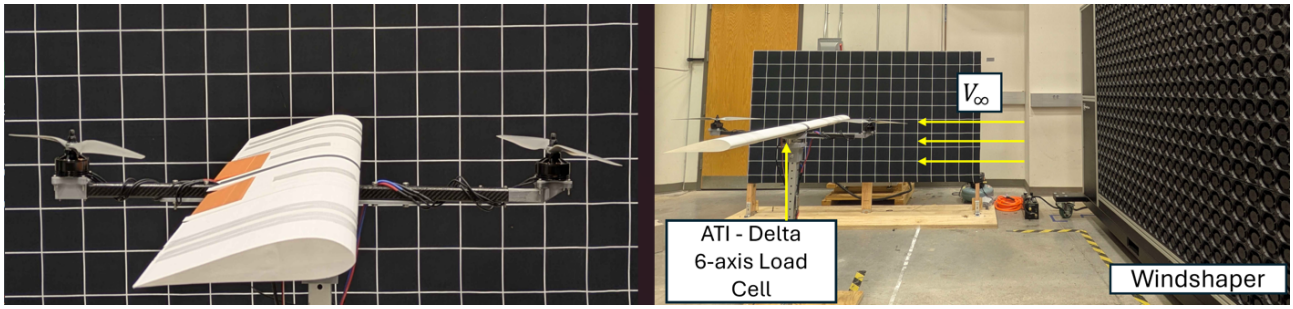


Figure 7 – Experimental setup in 7.9 ft $\times$ 6.3 ft WindShape®

placement within the WindShape® test section. The experimental setup was positioned at a distance of 1.5 Windshape lengths (L). As illustrated in Fig. 3., this distance is measured from the propeller tip when the propeller is aligned parallel to the flow.

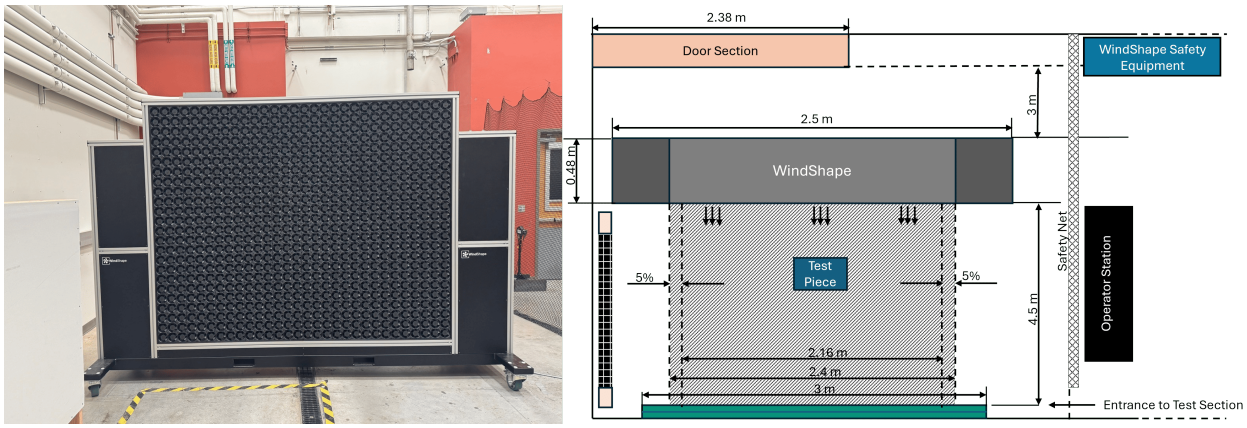


Figure 8 – 7.9 ft x 6.3 ft multifan-array wind generator (WindShaper) at OSU-Tulsa, front-view (left) and top-view drawing (right), representing the test section area.

The aforementioned parameters were varied to study the effects of the interaction and the changes in the control surface effectiveness. The parameters, their corresponding test points, and test sizes used to develop the test matrix, are summarized as follows:

- Boom distance (x_b): [1.4R, 2R] - (2 $\times$ 1)
- Propeller height (h_r): [0.23R, 0.5R] - (2 $\times$ 1)
- RPM (N): [4900, 4050, 2600] - (3 $\times$ 1)
- Freestream velocity (V_∞): [10, 20, 25] kts - (3 $\times$ 1)
- Control surface deflection (δ): $[-30°, -15°, 0°, +15°, +30°]$ - (5 $\times$ 1)

The test matrix was designed such that the test points for V_∞ are closer to trim conditions for S2F-X200 (x_b = 2 R). For each freestream velocity, a corresponding propeller rotational speed closer to trim is enforced. For example, the trim condition at V_∞ = 10 kts corresponds to $\approx$ 4900 RPM. This results in a total to a test size of $[3 \times 1]$. This ensures that all tested configurations reflect physically realizable operating points and reduces the experimental space to aerodynamically consistent combinations of velocity and RPM. For each x_b, tests are conducted across all combinations of h_r, V_∞ (and its corresponding RPM), and δ, combining to $2 \times 2 \times 3 = 12$ test cases. In total, this results in $12 \times 5 = 60$ tests across all boom distances. In all the x_b cases, only the boom length for the forward propellers were altered whereas the x_b for the rear propelllers remained constant throughout the experiments at x_b = 1.4R.

3.3 Wake Skew Validation

A smoke-visualization study was conducted to provide a qualitative and semi-quantitative check of the fore-propeller wake skew under transition-representative operating conditions. The purpose of

this test was not to reconstruct the full three-dimensional velocity field, but rather to verify that the propeller wake is redirected downstream toward the wing and control-surface region as freestream velocity increases. This behavior is central to the interpretation of the propeller-wing active tests, since a skewed wake changes the local velocity direction, effective angle of attack, and dynamic pressure experienced by the downstream lifting surface.

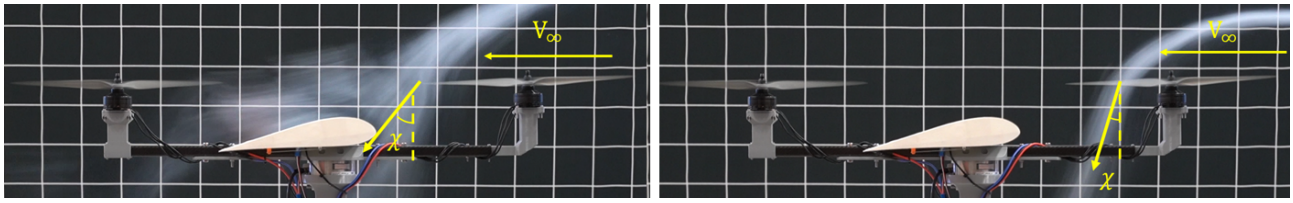
Smoke was introduced near the fore lift propeller and imaged from the side of the test section for the Case II ($x_b = 2R$, $h_r = 0.5R$) geometry. The left column of Fig. 9 shows smoke introduced near the propeller tip region, while the right column shows smoke introduced closer to the central portion of the wake. Three transition-representative conditions were considered: $V_\infty = 10$ kts at 4900 RPM, $V_\infty = 20$ kts at 4050 RPM, and $V_\infty = 25$ kts at 2600 RPM. These conditions correspond to increasing freestream velocity and decreasing lift-propeller rotational speed, consistent with the trim schedule used in the propeller-wing experiments.

The wake skew angle was estimated from the smoke images by measuring the orientation of the visible smoke trajectory relative to the nominal propeller axial-flow direction. The resulting experimental estimate, χ_{TEST}, was compared with the simulated wake skew angle, χ_{SIM}, obtained from the baseline propeller inflow model. The comparison is summarized in Table 3. The experimental uncertainty is estimated to be approximately $\pm 2.5^\circ$, based on the image resolution, smoke-line thickness, and manual extraction of the wake trajectory.

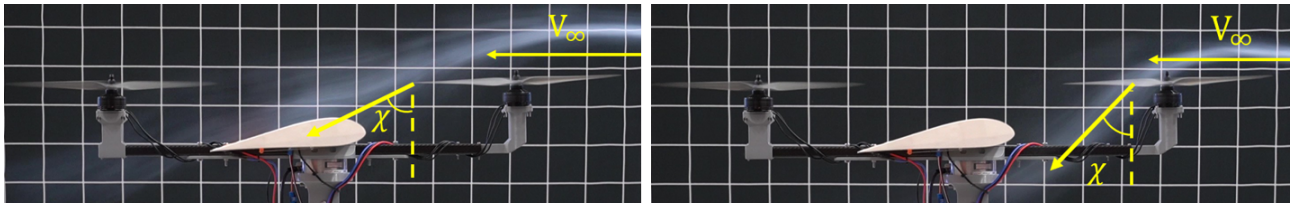
The results show the expected increase in wake skew with freestream velocity. At $V_\infty = 10$ kts and 4900 RPM, the wake remains more closely aligned with the propeller axial direction, with an experimentally measured skew angle of approximately 34°. At $V_\infty = 20$ kts and 4050 RPM, the wake is redirected substantially downstream, with $\chi_{TEST} \approx 67^\circ$. At $V_\infty = 25$ kts and 2600 RPM, the wake remains highly skewed, with $\chi_{TEST} \approx 71^\circ$. The simulated values capture the same trend, predicting an increase from 30.52° to 59.34° and then to 77.41° across the three operating points.

The agreement between χ_{SIM} and χ_{TEST} is sufficient for the intended purpose of this study: confirming that the fore-propeller wake is strongly skewed during transition and is convected toward the downstream wing. Differences between the simulated and measured skew angles are expected because the smoke visualization captures a finite-width, spatially nonuniform wake, while the simulation reports a representative wake angle from a reduced-order inflow model. Additional differences may arise from smoke injection location, wake curvature, local blockage from the wing-boom assembly, fan-array nonuniformity, and perspective effects in the side-view image.

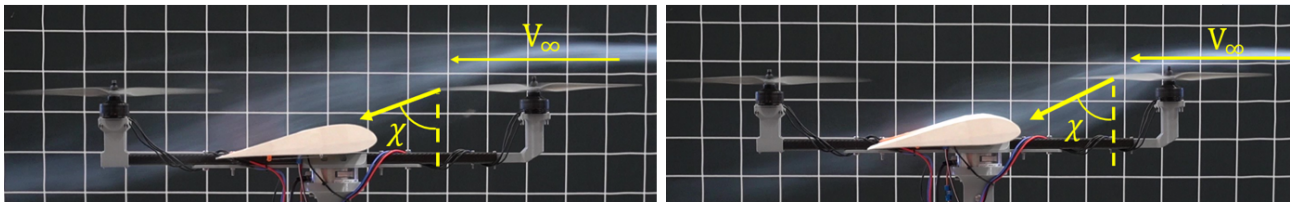
The visualizations in Fig. 9 indicate that the wake trajectory intersects the downstream wing and control-surface region for the tested transition conditions. Therefore, the propeller-wing active configuration should not be expected to equal a simple superposition of isolated propeller loads and clean-wing loads. Instead, the wing operates in a locally skewed and nonuniform propeller-induced flow field. This observation provides a physical basis for the interaction effects identified later in Sec. 4.2.2, particularly the reduction in measured vertical force relative to the non-interacting superposition model.



(a) Case II: 10 kts freestream velocity, 4900 RPM



(b) Case II: 20 kts freestream velocity, 4050 RPM



(c) Case II: 25 kts freestream velocity, 2600 RPM

Figure 9 – Smoke visualization of fore-propeller wake skew for the Case II geometry. The left column shows smoke introduced near the propeller tip region, and the right column shows smoke introduced near the central wake region. Rows correspond to transition-representative trim conditions at (a) $V_\infty = 10$ kts and 4900 RPM, (b) $V_\infty = 20$ kts and 4050 RPM, and (c) $V_\infty = 25$ kts and 2600 RPM.

Table 3 – Comparison of simulated χ_{SIM} and experimentally χ_{TEST} estimated wake skew angle for the Case II smoke-visualization conditions.

V_∞ [kts]	RPM	χ_{SIM} [deg]	χ_{TEST} [deg]
10	4900	30.52	34 (± 2.5)
20	4050	59.34	67 (± 2.5)
25	2600	77.41	71 (± 2.5)

4. Results

This section presents the experimental results in three subsections: isolated propeller experiments, propeller-wing experiments, and control surface effectiveness. In the first two subsections, only the test points corresponding to the 0° control-surface deflection cases are considered. The third subsection is dedicated to assessing the effect of the fore propeller on control surface effectiveness.

To establish appropriate reference cases for the simulation model, the isolated propeller measurements are first compared with computations from the existing BET model under identical operating conditions. Likewise, the *Propeller-Wing Baseline* configuration is replicated using strip theory, and the resulting predictions are compared with the corresponding experimental data.

The propeller-wing experiments are then further divided into four geometric sub-cases obtained by varying x_b and h_r from the test matrix described in Sec. 3.2. These sub-cases allow the influence of downstream propulsor placement relative to the wing to be examined in greater detail.

4.1 Isolated Propeller Experiments

The isolated propeller experiments were used to characterize the standalone force and moment response of the APC 16×5.5 MR lift propeller as a function of freestream velocity and rotational speed. The non-dimensional force and moment coefficients obtained from these tests are shown in

Fig. 10. Each data point was computed by averaging the measured response over the steady portion of the corresponding 10 sec PWM interval described in Sec. 3.1.

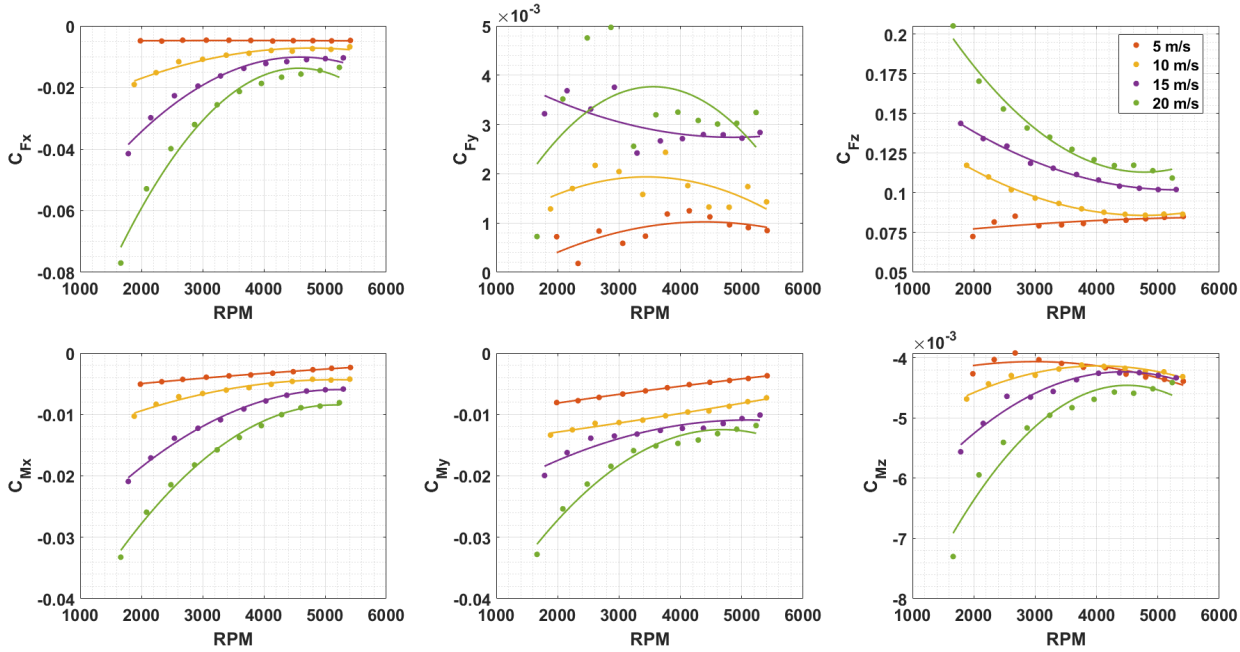


Figure 10 – Force and moment coefficients obtained from the isolated propeller tests at different freestream velocities.

The results show that the isolated propeller coefficients are most sensitive to freestream velocity at lower rotational speeds, where the advance ratio is larger. As RPM increases, the coefficient trends become more closely grouped across freestream conditions, indicating that the blade tangential velocity becomes dominant relative to the edgewise inflow component. The thrust coefficient, C_{F_z}, and torque coefficient, C_{M_z}, exhibit the clearest dependence on RPM and freestream velocity, while the lateral force coefficient, C_{F_y}, shows greater scatter. This scatter is attributed primarily to small installation asymmetries, load-cell alignment uncertainty, and nonuniformities in the inflow or propulsor mounting.

To support interpolation at the transition-representative test points, the isolated propeller data were fitted using second-order polynomial functions of RPM at each freestream velocity. Each fit was expressed in the form

$$y = p_1 \mathrm{RPM}^2 + p_2 \mathrm{RPM} + p_3, \tag{9}$$

where y represents the corresponding dimensional load or non-dimensional coefficient. The fitted coefficients, root mean square error (RMSE), and coefficient of determination (R^2) are provided in Tables A1 and A2 in Appendix A. The dimensional force and moment fits are also provided in Appendix A. These fitted maps were used to estimate isolated propeller loads at operating points that were not measured directly. For example, the isolated propeller loads at an intermediate combination of V_∞ and RPM were obtained by interpolation from the experimentally generated force and moment maps.

The isolated propeller measurements were also used to evaluate the baseline blade element theory (BET) propeller model. Initial comparisons showed a consistent offset between the BET predictions and the measured propeller loads. Therefore, the BET model was calibrated using a second-order correction factor, $k_c = f(\mathrm{RPM})$, applied to the model output. The calibrated BET predictions are compared with the isolated propeller measurements in Fig. 11. The corrected model captures the primary trends in the measured force and moment response and is used in the subsequent non-interacting superposition comparison.

The purpose of this calibration is not to introduce propeller-wing interaction effects into the simulation model. Instead, it ensures that the isolated propeller contribution is represented consistently before

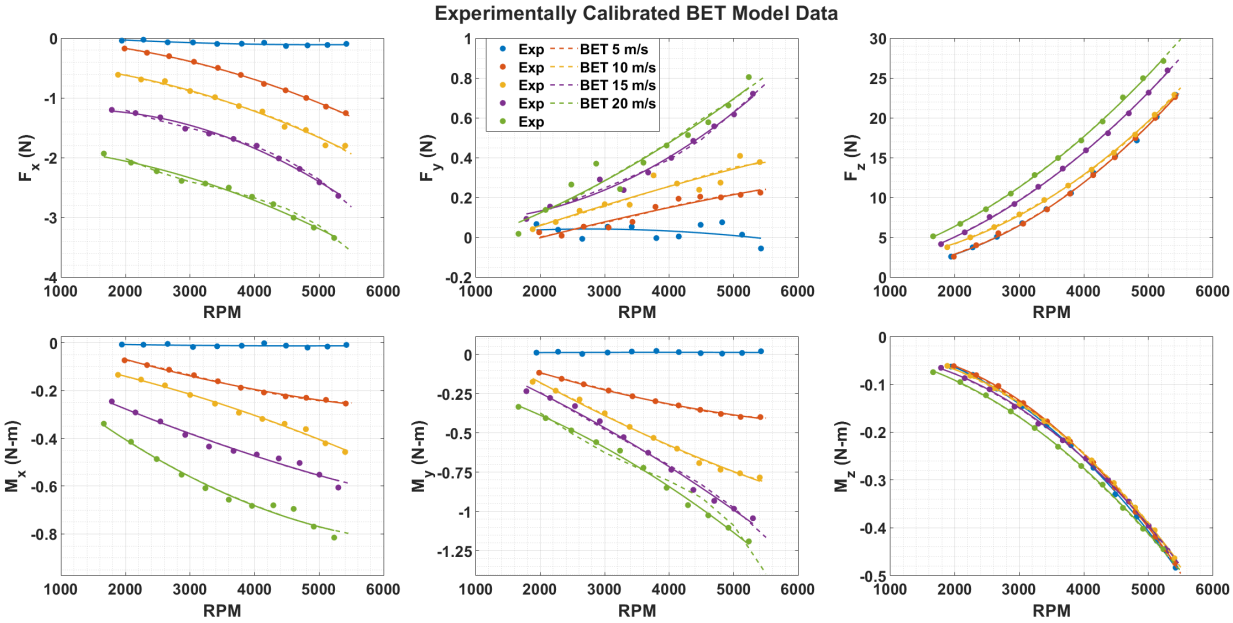


Figure 11 – Isolated propeller forces and moments compared with the calibrated BET model.

it is combined with the propeller-wing baseline model. Therefore, discrepancies observed later between the measured *Propeller-Wing Active* case and the non-interacting superposition model can be attributed more directly to propeller-wing interaction effects rather than to an uncorrected isolated propeller model.

4.2 Propeller-Wing Experiments

This section presents the results obtained from the propeller-wing experiments for the four geometric configurations considered in the test matrix. The configurations are denoted as Case I ($x_b = 2R$, $h_r = 0.23R$), Case II ($x_b = 2R$, $h_r = 0.5R$), Case III ($x_b = 1.4R$, $h_r = 0.23R$), and Case IV ($x_b = 1.4R$, $h_r = 0.5R$). For each configuration, the propeller-wing baseline case is first compared with the clean-wing strip-theory model. The propeller-wing active case is then compared with a non-interacting superposition model to identify aerodynamic interaction effects associated with fore-propeller operation.

Only the neutral control-surface condition, $\delta = 0°$, is considered in this section. Control-surface deflection effects are discussed separately in Sec. 4.3.

4.2.1 Propeller-Wing Baseline Comparison with Strip-Theory Model

The *Propeller-Wing Baseline* measurements were used to evaluate the strip-theory model for the installed wing-boom-propeller test article with the lift propellers inactive. This comparison establishes the clean-wing reference response before active propeller effects are considered. Since the propellers are installed but not rotating, the RPM labels in Figs. 12–15 are used only to identify the corresponding transition-trim test points. They do not represent active propeller operation in the baseline cases.

Figures 12–15 show that the strip-theory model captures the dominant clean-wing loading trends across the four configurations. The vertical-force component, F_z, is predicted with the closest agreement, indicating that the model captures the primary lifting behavior of the installed wing section. The pitching moment, M_y, also follows the measured trend reasonably well across the tested conditions, suggesting that the model provides an appropriate clean-wing reference for the later active-propeller comparison.

Larger discrepancies are observed in the axial and lateral force components and in selected rolling and yawing moment components. The strip-theory model predicts nearly zero lateral force for the nominally symmetric clean-wing condition, while the experimental measurements show nonzero offsets in F_y, M_x, and M_z. These offsets are attributed to installation effects that are not represented

in the idealized aerodynamic model, including small mounting asymmetries, load-cell alignment uncertainty, boom and inactive-propeller drag, and minor inflow nonuniformity from the fan-array test section.

The four baseline cases show broadly similar trends, which is expected because the propellers are inactive and the dominant measured loads are generated by the wing section and support hardware. Changes in x_b and h_r alter the installed geometry of the inactive propeller-boom assembly, but they do not introduce propeller-induced flow. Therefore, the baseline results indicate that the strip-theory model is adequate for representing the primary clean-wing contribution, while also defining the experimental offsets that must be considered when interpreting the active propeller-wing measurements.

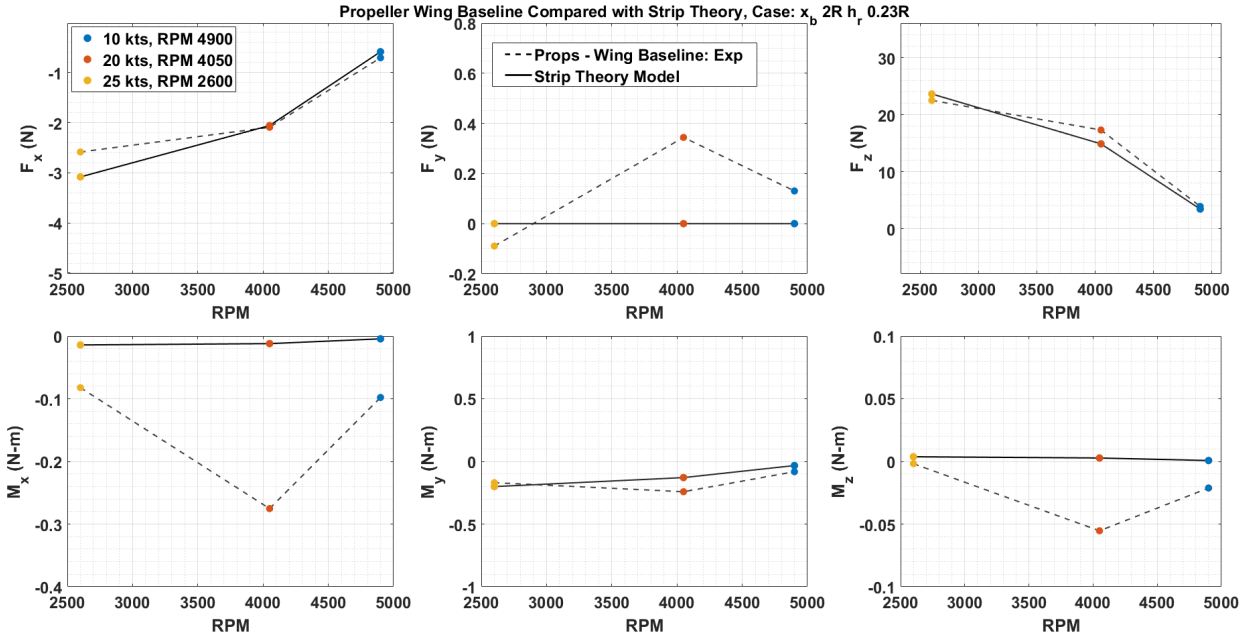


Figure 12 – Comparison between strip-theory prediction and propeller-wing baseline measurements for Case I ($x_b = 2R$, $h_r = 0.23R$).

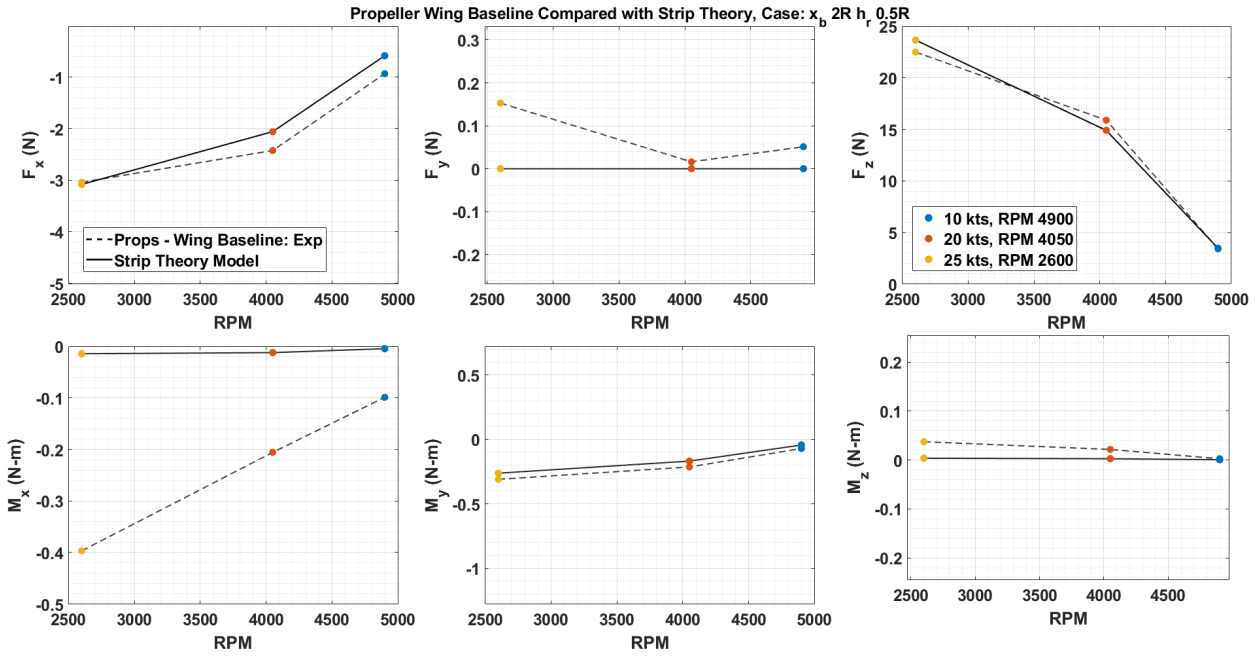


Figure 13 – Comparison between strip-theory prediction and propeller-wing baseline measurements for Case II ($x_b = 2R$, $h_r = 0.5R$).

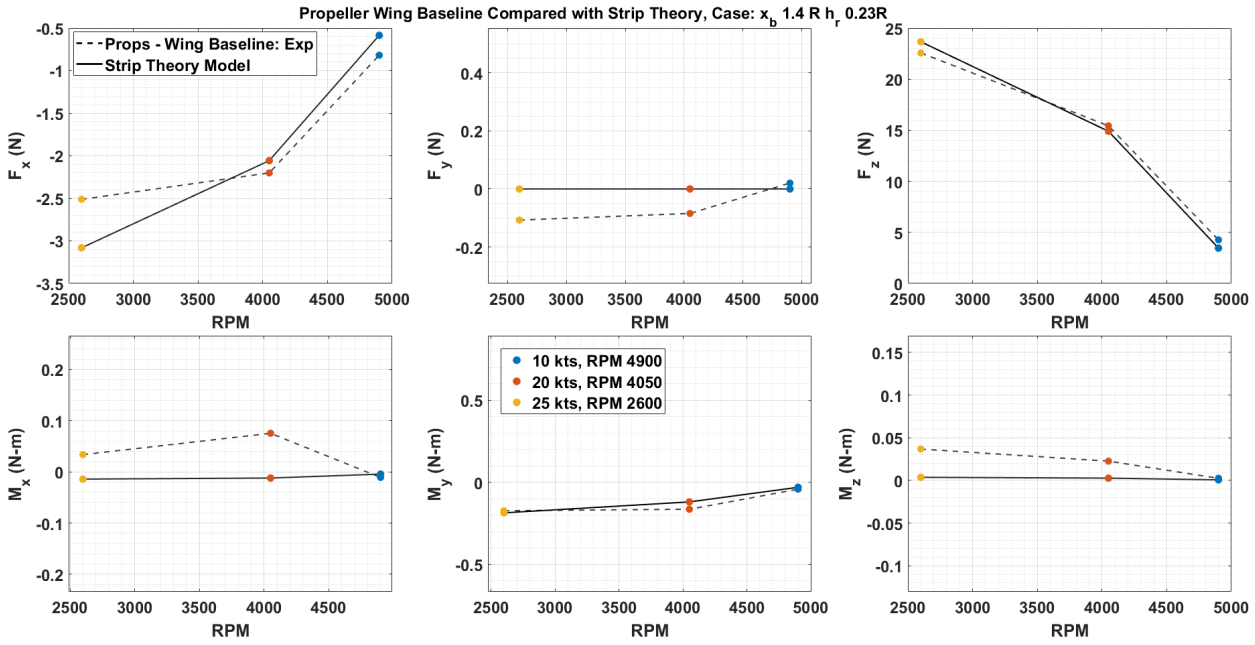


Figure 14 – Comparison between strip-theory prediction and propeller-wing baseline measurements for Case III ($x_b = 1.4R$, $h_r = 0.23R$).

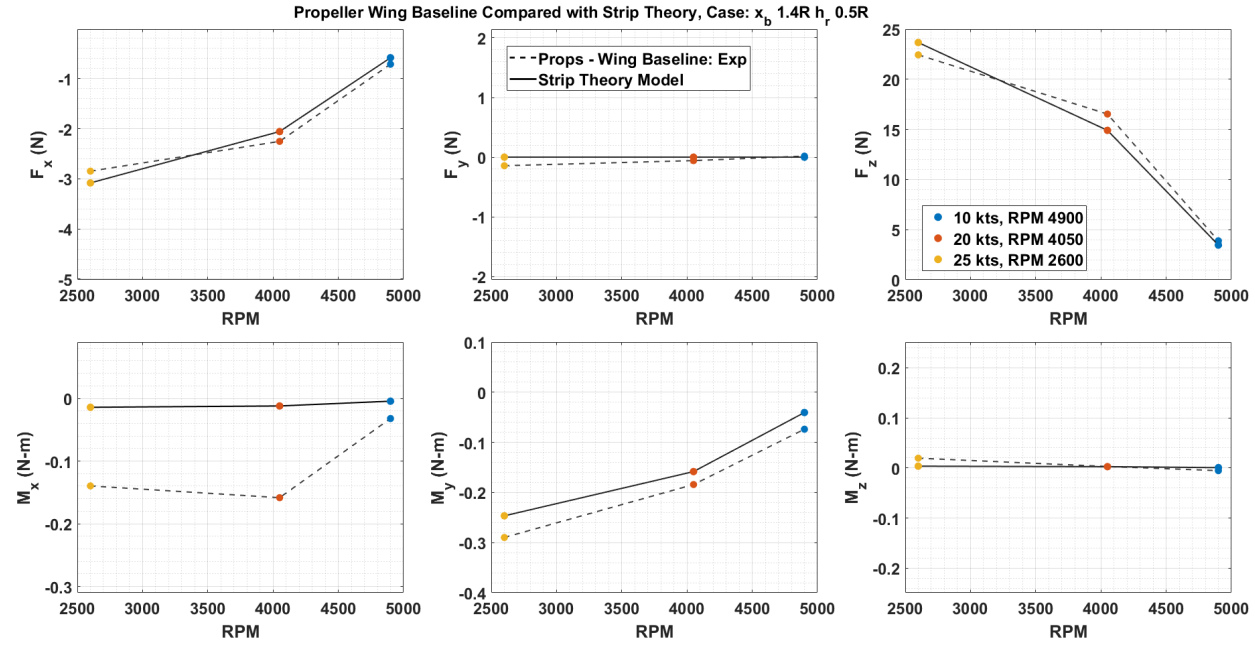


Figure 15 – Comparison between strip-theory prediction and propeller-wing baseline measurements for Case IV ($x_b = 1.4R$, $h_r = 0.5R$).

4.2.2 Propeller-Wing Active Case Comparison with Simulation Model

In this section, the *Propeller-Wing Active* measurements are compared against a non-interacting superposition of the independently modeled propeller and wing responses. The underlying hypothesis is that, if propeller-wing interaction effects are small, the total active propeller-wing loads can be approximated by adding the isolated propeller loads to the propeller-wing baseline loads. This non-interacting estimate is expressed as

$$\sum \mathbf{F}_{sup} = \mathbf{F}_{PW,baseline} + \mathbf{F}_{prop,isolated} \qquad \sum \mathbf{M}_{sup} = \mathbf{M}_{PW,baseline} + \mathbf{M}_{prop,isolated} \tag{10}$$

where the subscript sup denotes the superposed non-interacting prediction. The comparison between this estimate and the measured *Propeller-Wing Active* case provides a direct indication of

aerodynamic interaction effects that are not captured by the uncoupled blade-element and strip-theory models.

Figures 16–19 compare the measured active propeller-wing response with the corresponding superposed prediction for the four geometric configurations. Across all cases, the most consistent discrepancy appears in the vertical-force component, F_z. The superposed model generally predicts a larger F_z than is measured in the active propeller-wing configuration. This indicates that the combined propeller-wing system produces less vertical force than would be expected from a simple addition of the isolated propeller and baseline wing contributions. Therefore, the fore-propeller wake does not act as an independent load source; instead, it modifies the aerodynamic loading on the downstream wing.

This reduction in measured F_z is consistent with the wake-skew behavior observed in Sec. 3.3. As the freestream velocity increases during transition, the propeller wake becomes increasingly skewed and is convected downstream toward the wing and control-surface region. The resulting flow field is spatially nonuniform and contains both axial and transverse velocity components. When this skewed wake impinges on the wing, it can reduce the local effective angle of attack over portions of the lifting surface, alter the local dynamic pressure distribution, and disturb the nominal circulation pattern assumed by the clean-wing strip-theory model. The observed F_z deficit is therefore interpreted as a lift reduction associated with propeller-wing interaction rather than a deficiency in the isolated propeller or baseline wing models alone.

The magnitude of this discrepancy depends on propeller placement. Cases I and II place the fore propeller at $x_b = 2R$, while Cases III and IV place it closer to the wing at $x_b = 1.4R$. The closer longitudinal placement generally produces stronger departures between the measured active response and the superposed estimate, particularly in F_z and selected moment components. This trend is consistent with a more direct interaction between the skewed propeller wake and the wing when the propeller is positioned closer to the lifting surface. The vertical offset, h_r, also affects the interaction by changing the portion of the wake that intersects the wing and control-surface region.

The remaining force and moment components show additional evidence of interaction, but with less uniform trends than F_z. The lateral force, F_y, and rolling/yawing moment components are sensitive to small asymmetries, propeller rotation direction, wake swirl, and installation effects. The pitching moment, M_y, also changes between the superposed and active cases, indicating that the propeller wake changes not only the net vertical loading but also the chordwise distribution of pressure over

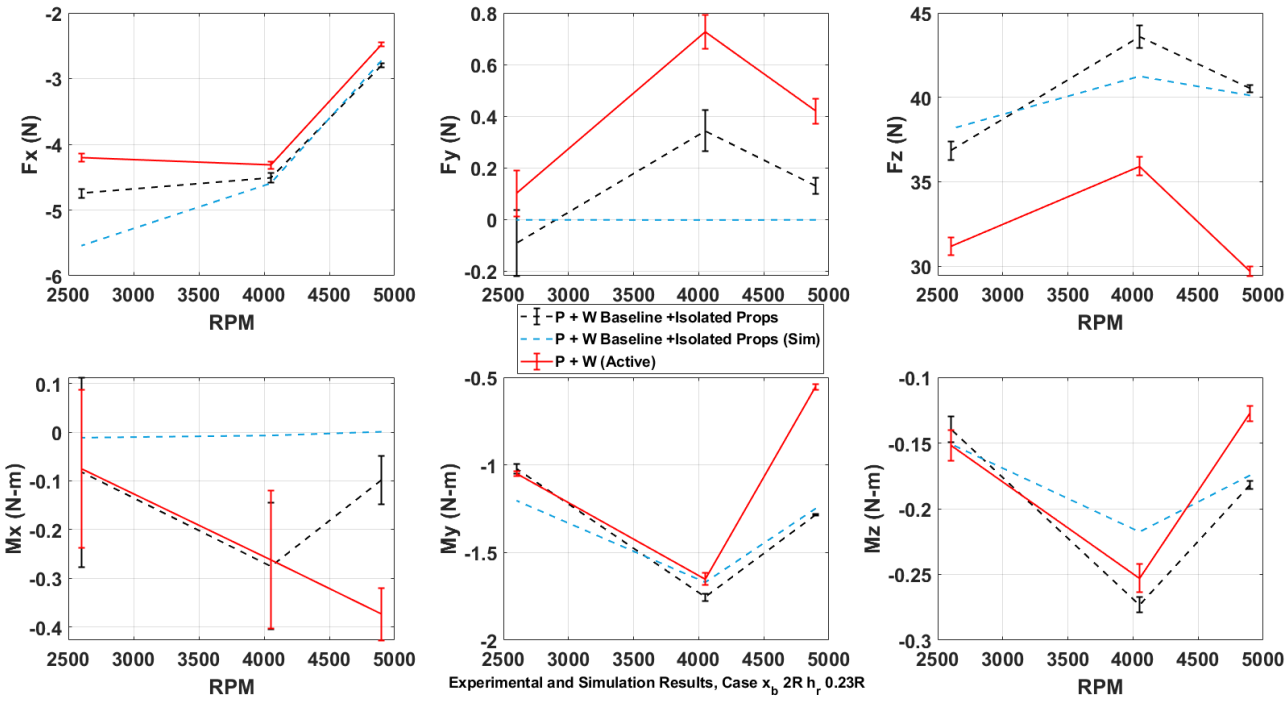


Figure 16 – Comparison between simulation and experiment for Case I

the wing. These trends reinforce that the active propeller-wing configuration cannot be represented accurately by uncoupled isolated-propeller and clean-wing models.

Overall, the active-case comparisons show that fore lift-propeller operation produces a measurable reduction in vertical force relative to the non-interacting superposition model. The wake-skew validation provides a physical explanation for this behavior: under transition-representative conditions, the propeller wake is redirected into the downstream wing region, producing a coupled flow field that changes the wing loading and associated moments. These results motivate the development of future reduced-order interaction corrections that modify the local wing-strip velocity, effective angle of attack, and dynamic pressure based on propeller operating condition and placement.

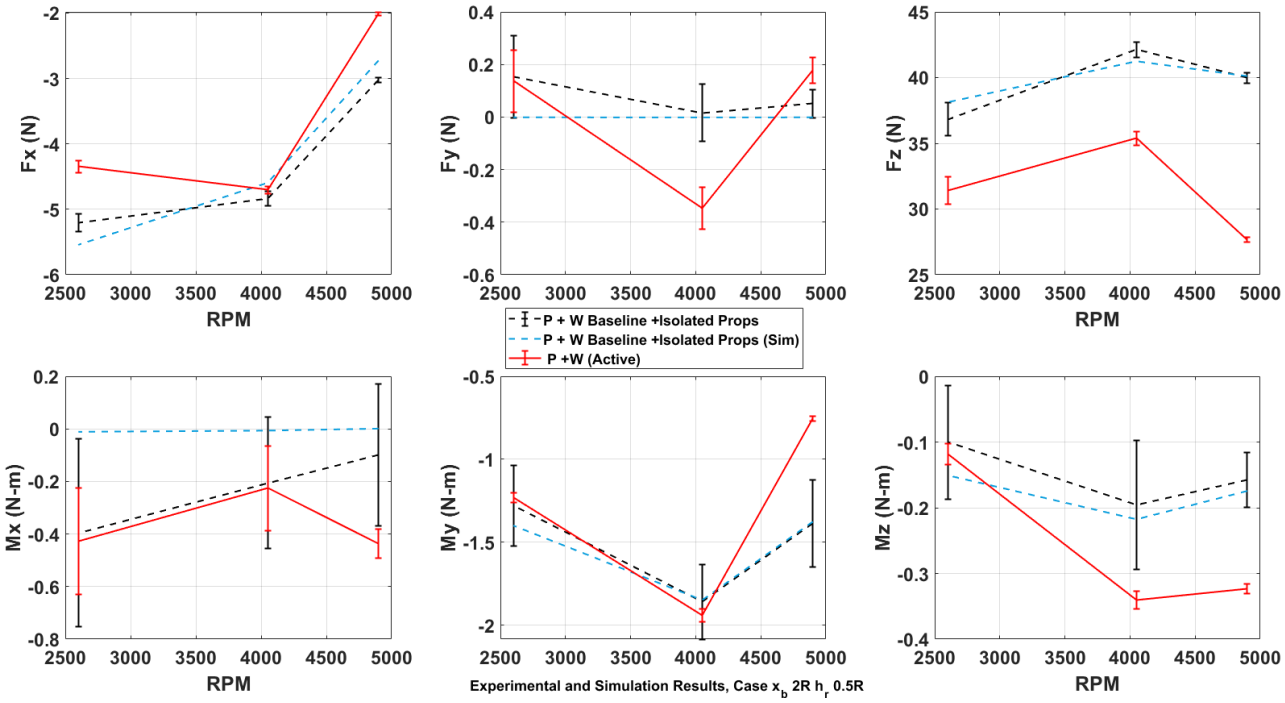


Figure 17 – Comparison between simulation and experiment for Case II

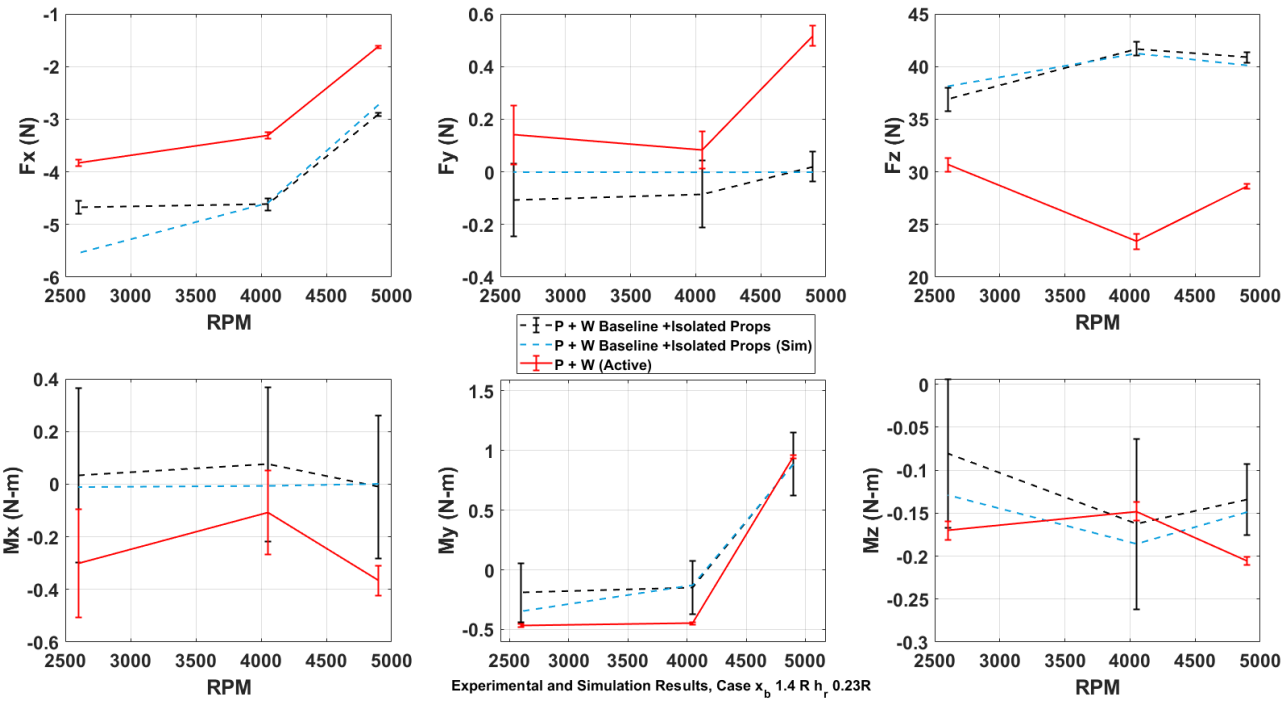


Figure 18 – Comparison between simulation and experiment for Case III

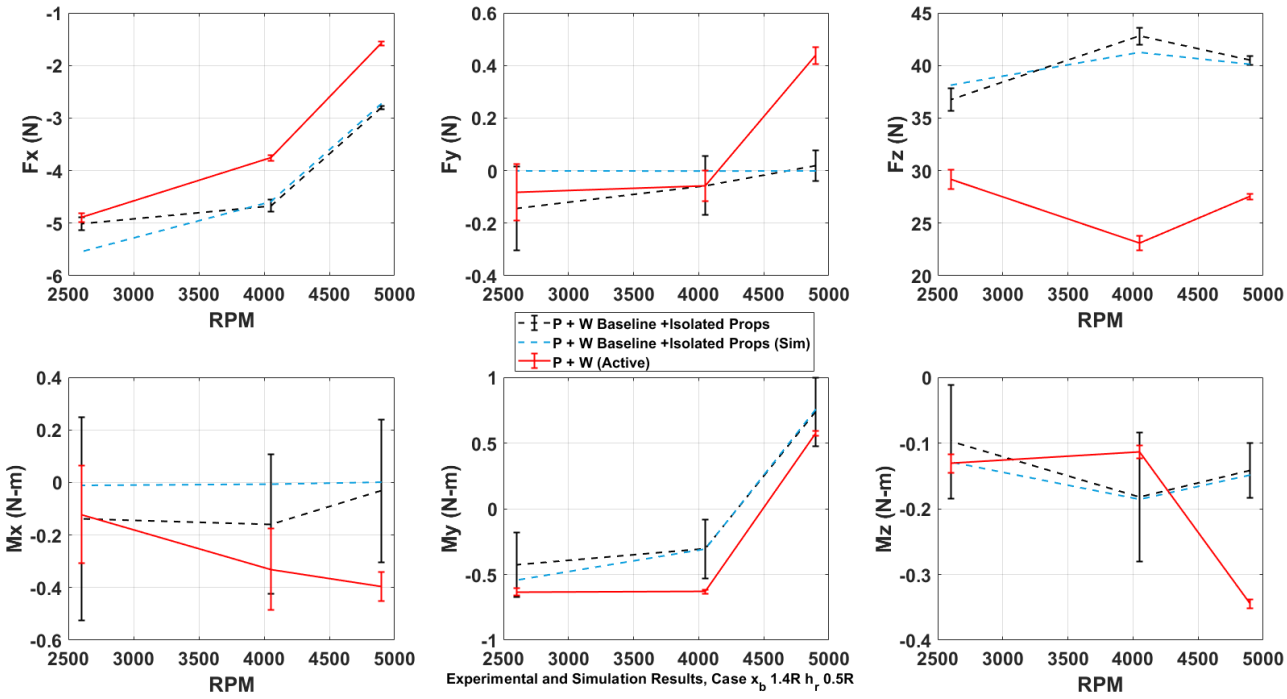


Figure 19 – Comparison between simulation and experiment for Case IV

4.3 Control Surface Effectiveness

To assess the effect of propeller wake impingement on the control surfaces, the propeller-wing configuration was tested at control-surface deflections of $\delta = [-30°, -15°, 0°, +15°, +30°]$. Both left and right control surfaces were deflected equally, corresponding to a flap-like control input. As shown in Fig. 3., the control surfaces are located downstream of the fore lift propeller. Based on the projected propeller disk diameter, the fore-propeller wake overlaps approximately 80% of the left and right control-surface region. This placement suggests that propeller operation may alter the local velocity, effective angle of attack, and dynamic pressure experienced by the deflected control surfaces.

Control-surface effectiveness was evaluated using the axial-force, vertical-force, and pitching-moment responses. The measured forces and moments were converted into equivalent aerodynamic coefficients according to

$$C_{F_x} = \frac{2F_x}{\rho V_\infty^2 S}, \qquad C_{F_z} = \frac{2F_z}{\rho V_\infty^2 S}, \qquad C_{M_y} = \frac{2M_y}{\rho V_\infty^2 S c}, \tag{11}$$

where S is the wing reference area, c is the reference chord, and V_∞ is the freestream velocity. For each coefficient, the control-surface increment was then computed relative to the neutral-deflection condition at the same freestream velocity, propeller speed, and geometric configuration:

$$\Delta C_i(\delta) = C_i(\delta) - C_i(0°), \qquad C_i \in \{C_{F_x}, C_{F_z}, C_{M_y}\}. \tag{12}$$

This normalization removes the static force and moment offset associated with each test condition and isolates the incremental response due to control-surface deflection. The propeller-wing baseline case corresponds to the installed but inactive propellers, while the propeller-wing active case corresponds to operating lift propellers at the transition-representative trim condition. Differences between the baseline and active increments therefore indicate changes in control-surface effectiveness associated with fore-propeller operation.

Figures 20–23 show the control-surface coefficient increments for the four propeller-wing configurations. Across all cases, the vertical-force increment, ΔC_{F_z}, retains the expected first-order dependence on deflection. Negative deflections produce negative vertical-force increments, while positive deflections produce positive increments. This indicates that the flap-like control input remains effective even with the fore lift propeller operating. However, the propeller-wing active cases do not collapse onto the baseline cases, showing that propeller operation modifies the local flow environment over the control-surface region.

The axial-force increment, ΔC_{F_x}, shows a weaker and less systematic dependence on propeller operation. The largest changes occur at the largest positive and negative deflections, while the response remains near zero at the neutral condition by construction. In several cases, the active-propeller response changes the magnitude of the axial-force increment relative to the baseline, but the trend is less consistent than the vertical-force and pitching-moment responses. Therefore, ΔC_{F_x} is treated primarily as supporting evidence that the propeller wake modifies the local loading, rather than as the primary indicator of control-surface effectiveness.

The clearest effect of propeller operation appears in the pitching-moment increment, ΔC_{M_y}. For the propeller-wing baseline cases, the pitching-moment response is generally monotonic with deflection, with negative deflections producing negative moment increments and positive deflections producing positive moment increments. When the lift propellers are active, the pitching-moment response is modified in both slope and magnitude. This behavior is most apparent in Cases I and III, where the active-propeller curves show reduced moment increments relative to the baseline response over portions of the deflection range. These results indicate that the fore-propeller wake changes the effective incidence and/or dynamic pressure over the deflected control-surface region.

The comparison between configurations suggests that the interaction is sensitive to propeller placement. Cases I and II have the same longitudinal placement, $x_b = 2R$, but different vertical offsets. Increasing the vertical offset from $h_r = 0.23R$ to $h_r = 0.5R$ generally reduces the separation between the baseline and active pitching-moment trends, suggesting a weaker wake influence on the control-surface region. Cases III and IV place the fore propeller closer to the wing, at $x_b = 1.4R$. These cases show stronger changes in the vertical-force and pitching-moment increments at selected speeds, consistent with a more direct interaction between the skewed propeller wake and the downstream control surface.

The speed dependence is not strictly monotonic because the transition-trim conditions combine changes in freestream velocity and propeller rotational speed. As freestream velocity increases, the wake skew angle increases and the projected wake location over the wing changes. At the same time, the commanded lift-propeller speed decreases with increasing freestream velocity. The measured control-surface increments therefore reflect the combined effects of wake skew, induced velocity, propeller placement, and control-surface deflection. Overall, the data show that fore lift-propeller operation modifies control-surface effectiveness in a placement- and trim-dependent manner, with the most consistent changes appearing in the pitching-moment response.

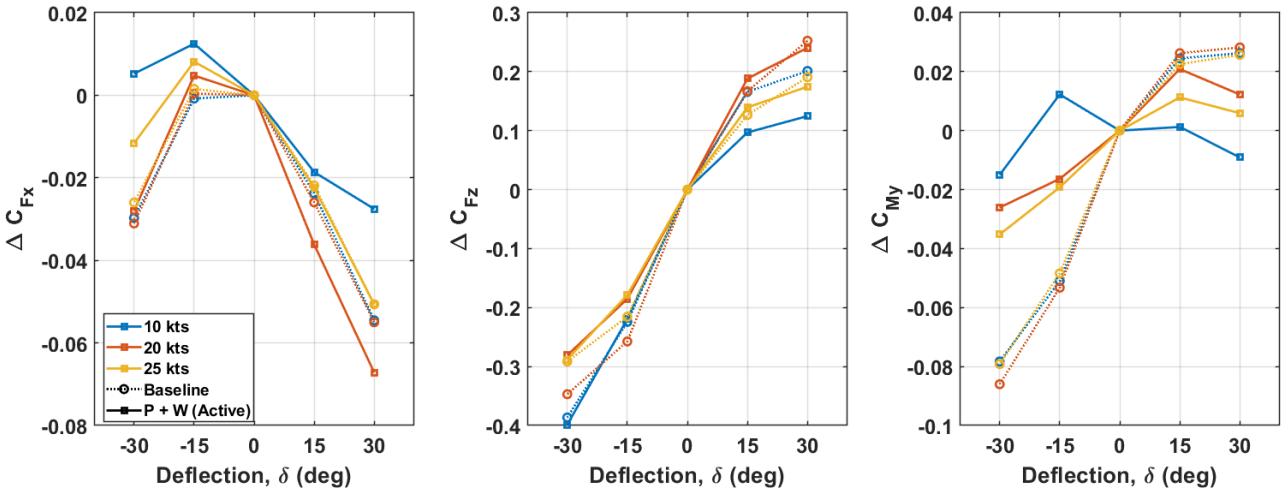


Figure 20 – Control surface deflections, Case I (x_b 2R, h_r 0.23R)

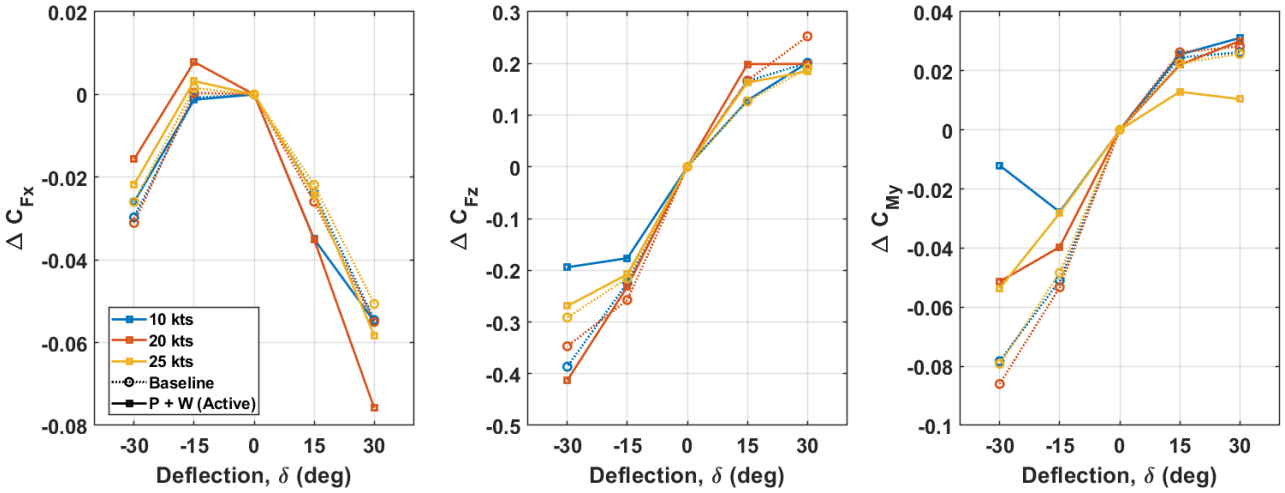


Figure 21 – Control surface deflections, Case II (x_b 2R, h_r 0.5R)

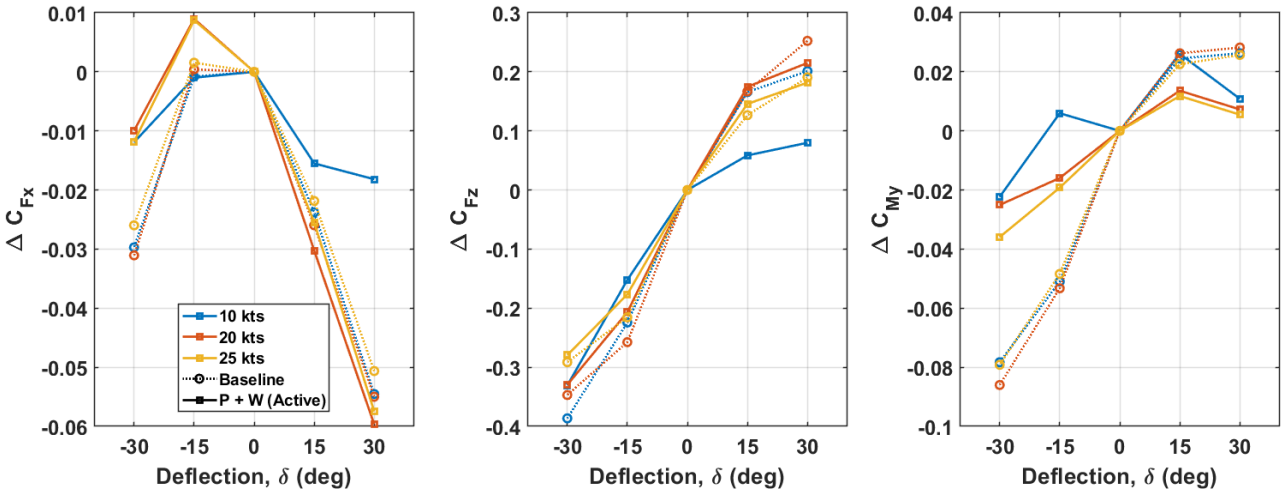


Figure 22 – Control surface deflections, Case III (x_b 1.4R, h_r 0.23R)

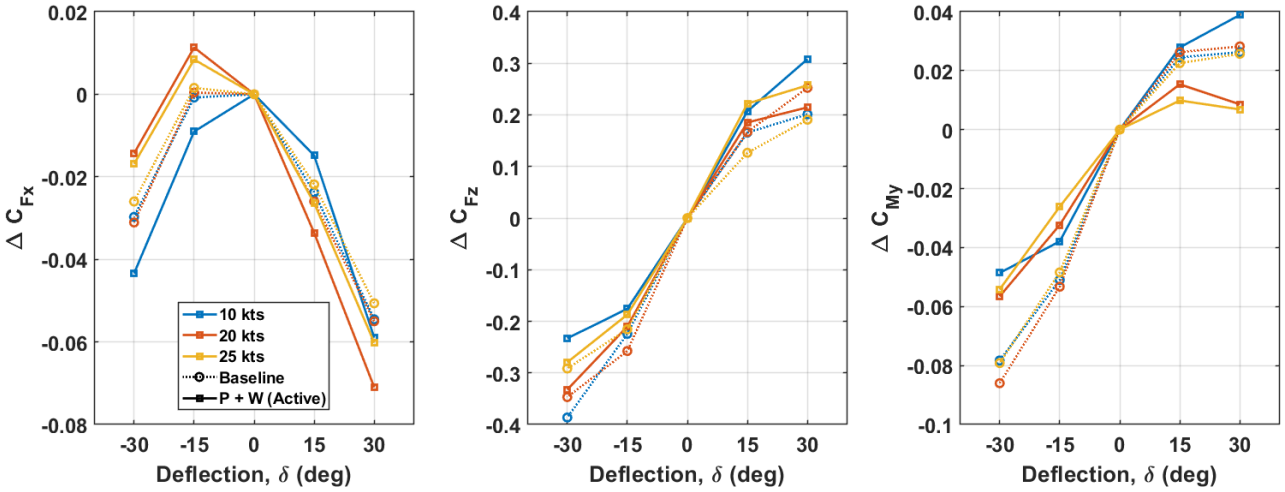


Figure 23 – Control surface deflections, Case IV (x_b 1.4R, h_r 0.5R)

5. Concluding Remarks

This paper experimentally characterized fore lift-propeller/wing aerodynamic interactions for a subscale lift-plus-cruise VTOL UAV under transition-representative operating conditions. The S2F-X200 configuration was used as the reference vehicle, and a representative wing-boom-propeller assembly was tested in WindShape® fan-array facilities using an ATI Delta six-axis force and moment balance. The experimental campaign included isolated propeller tests, propeller-wing baseline tests with inactive propellers, propeller-wing active tests with operating lift propellers, and control-surface deflection sweeps.

The isolated propeller experiments provided standalone force and moment maps for the APC 16×5.5 MR(P) lift propeller as functions of freestream velocity and rotational speed. These data were used to calibrate the baseline BET propeller model before combining it with the clean-wing strip-theory model. The propeller-wing baseline cases showed that the strip-theory model captured the dominant clean-wing loading trends, particularly in vertical force and pitching moment. Remaining offsets in lateral force and selected moment components were attributed primarily to installation asymmetries, load-cell alignment uncertainty, and test-section effects.

Smoke visualization confirmed that the fore lift-propeller wake becomes strongly skewed under transition-representative conditions. The measured wake skew angles followed the same trend as the simulated wake-skew estimates, increasing as freestream velocity increased and lift-propeller rotational speed decreased. These observations showed that the propeller wake is convected into the downstream wing and control-surface region, supporting the interpretation that the active propeller-wing configuration cannot be represented as a simple superposition of isolated propeller and clean-wing loads.

The active propeller-wing measurements showed a consistent reduction in vertical force relative to the non-interacting superposition model. This result indicates that fore lift-propeller operation modifies the aerodynamic loading on the downstream wing rather than acting only as an independent propulsive load source. The observed vertical-force deficit is consistent with a skewed, nonuniform propeller wake altering the local effective angle of attack, dynamic pressure distribution, and circulation over the wing. The magnitude of the discrepancy varied with propeller placement, indicating that both longitudinal and vertical fore-propeller position influence the strength of the interaction.

Control-surface deflection tests further showed that propeller operation modifies the incremental aerodynamic response of the downstream control surfaces. The vertical-force increments retained the expected first-order dependence on deflection, indicating that the flap-like control input remained effective. However, the propeller-wing active cases did not collapse onto the baseline cases, and the clearest changes appeared in the pitching-moment increments. These results indicate that fore-propeller wake impingement affects not only the net wing loading but also the control-surface effectiveness and chordwise loading distribution during transition.

Overall, the results demonstrate that lift-propeller/wing interaction effects are measurable for lift-plus-cruise configurations during transition and are not captured by clean-wing or uncoupled propeller models. The data provide an experimental basis for future reduced-order interaction modeling in which local wing-strip velocity, effective angle of attack, and dynamic pressure are modified as functions of propeller operating condition, wake skew, and propeller placement. Such corrections are expected to improve transition-regime flight simulation, trim prediction, and control-law development for lift-plus-cruise VTOL aircraft.

6. Acknowledgments

This research was partially funded by the US Economic Development Administration Grant 08-69-05693, the George Kaiser Family Foundation, and Tulsa Innovation Labs.

7. Contact Author Email Address

The corresponding author for this paper is Pratibha Bhandari, pratibha.bhandari@okstate.edu, Cell: (918) 888-0441| Address: 526 N Elgin Ave, Tulsa, OK, USA 74106.

8. Copyright Statement

The authors confirm that they, and/or their company or organization, hold copyright on all of the original material included in this paper. The authors also confirm that they have obtained permission,

from the copyright holder of any third party material included in this paper, to publish it as part of their paper. The authors confirm that they give permission, or have obtained permission from the copyright holder of this paper, for the publication and distribution of this paper as part of the ICAS proceedings or as individual off-prints from the proceedings.

References

[1] Ross Heidersbach, Anthony P Pisano, Alex Spens, Victoria Murnieks, Dhuree Seth, Matthew McCrink, and Jeffrey P Bons. Geometric effects on the aerodynamic interactions of a wing-propeller combination in hover flight. In *AIAA SciTech 2024 Forum*, page 1725, 2024.

[2] Pooneh Aref, Mehdi Ghoreyshi, Adam Jirasek, Matthew J Satchell, and Keith Bergeron. Computational study of propeller–wing aerodynamic interaction. *Aerospace*, 5(3):79, 2018.

[3] R.H. Stone. Aerodynamic Modeling of the Wing-Propeller Interaction for a Tail-Sitter Unmanned Air Vehicle. *AIAA Journal of Aircraft*, 45(1):198–210, 2008.

[4] Baizura Bohari, Quentin Borlon, Murat Bronz, and Emmanuel Benard. Aerodynamic model of propeller–wing interaction for distributed propeller aircraft concept. *Proceedings of the Institution of Mechanical Engineers, Part G: Journal of Aerospace Engineering*, 234(10):1688–1705, 2020.

[5] Joon W Lim. Fundamental Investigation of Proprotor and Wing Interactions in Tiltrotor Aircraft. In *Proceedings of the 75th Annual Vertical Flight Society Forum and Technology Display, Philadelphia, PA, USA*, pages 13–16, 2019.

[6] Shreyas Srivathsan and Juergen Rauleder. Experimental Wind Tunnel Investigation on Propeller-Wing Interactional Aerodynamics. In *AIAA SCITECH 2023 Forum*, page 1752, 2023.

[7] Fort F Felker and Jeffrey S Light. Rotor/wing Aerodynamic Interactions in Hover. In *Annual Forum of the American Helicopter Society*, number NASA-TM-88255, 1986.

[8] Larry A Young and Michael R Derby. Rotor/wing interactions in hover. Technical report, 2002.

[9] Jean-Paul Reddinger, Raphaël Perret, Justin N Martin, Christian Brackbill, and Laurent Binet. Stability and control sensitivity of a lift-plus-cruise evtol aircraft to trim strategy and modeling parameters. In *ERF 2024 European Rotorcraft Forum*, 2024.

[10] Oliver Westcott, Robert Entwistle, and Swathi Krishna. Propeller-wing interactions of a lift+ cruise evtol configuration during transition. 2025.

[11] Jinggen Zhao. *Dynamic Wake Distortion Model for Helicopter Maneuvering Flight*. PhD thesis, Georgia Institute of Technology, Atlanta, GA, USA, March 2005.

[12] M. McVeigh. The V-22 Tilt-rotor Large-scale Rotor Performance/Wing Download Test and Comparison with Theory. *Vertica*, 10(3):281–297, 1986.

[13] M. Kraenzler, M. Schmitt, and E. Stumpf. Conceptual Design Study on Electrical Vertical Take Off and Landing Aircraft for Urban Air Mobility Applications. In *AIAA Aviation 2019 Forum*, page 3124, 2019.

[14] Frédéric Blondel and Marie Cathelain. An Alternative Form of the Super-Gaussian Wind Turbine Wake Model. *Wind Energy Science Discussions*, 2020:1–16, 2020.

[15] B.W. McCormick. *Aerodynamics of V/STOL Flight*. Academic Press, New York, 1st edition, 1969.

[16] J.W. Cook and J. Hauser. A Strip Theory Approach to Dynamic Modeling of Tiltwing eVTOL Aircraft. In *AIAA SCITECH Forum 2021*, (virtual event), 2021. AIAA-2021-1720.

[17] A. Comer, Z. Atkinson, P. Bhandari, Z. Miller, and Harp E. Development of a Simulation to Flight Workflow for Subscale Flight Testing of Experimental Control Laws. In *AIAA SCITECH 2026 Forum*, Orlando, FL, January 2026. AIAA-2026-2063.

[18] I. Chakraborty and A. Mishra. Sizing and Analysis of a Lift-Plus-Cruise Aircraft with Electrified Propulsion. *AIAA Journal of Aircraft*, 60(3), 2023.

[19] Z. Atkinson, A.M. Comer, A. Marion, G. Sharma, S. Shahjahan, and T. Wilson. Multi-Fidelity Validation of Control Surface Deflection Predictions Using FlightStream. In *AIAA SCITECH 2026 Forum*, Orlando, FL, January 2026. AIAA-2026-2810.

[20] Mark Drela. Xfoil: An analysis and design system for low reynolds number airfoils. In *Low Reynolds number aerodynamics*, pages 1–12. Springer, 1989.

[21] ATI. Ati-f/t sensor:delta. Online: `https://www.ati-ia.com/products/ft/ft_models.aspx?id=delta`, 2026.

[22] Gordon J Leishman. *Principles of Helicopter Aerodynamics with CD extra*. Cambridge university press, 2006.

[23] Nikolas S Zawodny, Kyle A Pascioni, and Christopher S Thurman. An overview of the proprotor perfor-

mance test in the 14-by 22-foot subsonic tunnel. In *The Vertical Flight Society's 79th Annual Forum & Technology Display*, 2023.

A Polynomial Fit Data

Table A1 – Quadratic polynomial fit coefficients for C_{F_x}, C_{F_y}, and C_{F_z} as functions of RPM.

Coefficient	V_∞ [m/s]	p_1	p_2	p_3	RMSE	R^2
C_{F_x}	0	2.0979×10^{-11}	8.6435×10^{-9}	-0.0011	0.0002	0.5471
	5	-2.7626×10^{-11}	1.9929×10^{-7}	-0.0051	0.0001	0.0842
	10	-1.2904×10^{-9}	1.2283×10^{-5}	-0.0364	0.0009	0.9586
	15	-3.6115×10^{-9}	3.3158×10^{-5}	-0.0862	0.0018	0.9740
	20	-6.8628×10^{-9}	6.2784×10^{-5}	-0.1573	0.0032	0.9792
C_{F_y}	0	1.9604×10^{-10}	-1.7959×10^{-6}	0.0041	0.0004	0.5786
	5	-1.0739×10^{-10}	9.4393×10^{-7}	-0.0011	0.0002	0.4711
	10	-1.6975×10^{-10}	1.1681×10^{-6}	-7.3052×10^{-5}	0.0003	0.3154
	15	8.9515×10^{-11}	-8.7049×10^{-7}	0.0049	0.0004	0.4546
	20	-4.3720×10^{-10}	3.1102×10^{-6}	-0.0018	0.0011	0.2226
C_{F_z}	0	-1.6881×10^{-10}	3.3655×10^{-6}	0.0716	0.0014	0.8008
	5	-3.9251×10^{-10}	4.9731×10^{-6}	0.0690	0.0031	0.4376
	10	3.6967×10^{-9}	-3.5322×10^{-5}	0.1702	0.0007	0.9966
	15	3.3703×10^{-9}	-3.5685×10^{-5}	0.1964	0.0012	0.9945
	20	8.6729×10^{-9}	-8.2846×10^{-5}	0.3110	0.0051	0.9753

Table A2 – Quadratic polynomial fit coefficients for C_{M_x}, C_{M_y}, and C_{M_z} as functions of RPM.

Coefficient	V_∞ [m/s]	p_1	p_2	p_3	RMSE	R^2
C_{Mx}	0	-2.1599×10^{-11}	2.6921×10^{-7}	-0.0009	0.0001	0.5869
	5	-4.4960×10^{-11}	1.1000×10^{-6}	-0.0070	8.0079×10^{-5}	0.9935
	10	-5.0626×10^{-10}	5.2241×10^{-6}	-0.0178	0.0003	0.9775
	15	-1.2211×10^{-9}	1.2733×10^{-5}	-0.0392	0.0004	0.9924
	20	-1.9402×10^{-9}	2.0011×10^{-5}	-0.0600	0.0007	0.9942
C_{My}	0	6.6075×10^{-11}	-6.7139×10^{-7}	0.0018	0.0002	0.6549
	5	-5.2135×10^{-11}	1.6806×10^{-6}	-0.0113	7.3029×10^{-5}	0.9981
	10	4.6209×10^{-11}	1.2402×10^{-6}	-0.0155	0.0003	0.9828
	15	-6.8381×10^{-10}	6.9791×10^{-6}	-0.0287	0.0010	0.8975
	20	-2.0373×10^{-9}	1.9108×10^{-5}	-0.0573	0.0012	0.9725
C_{Mz}	0	-4.9902×10^{-11}	3.2805×10^{-7}	-0.0048	9.1743×10^{-5}	0.4436
	5	-6.6115×10^{-11}	3.9421×10^{-7}	-0.0047	8.4943×10^{-5}	0.7496
	10	-1.0613×10^{-10}	8.5871×10^{-7}	-0.0059	3.9823×10^{-5}	0.9509
	15	-1.7245×10^{-10}	1.5302×10^{-6}	-0.0076	9.6183×10^{-5}	0.9576
	20	-3.0575×10^{-10}	2.7498×10^{-6}	-0.0106	0.0002	0.9394

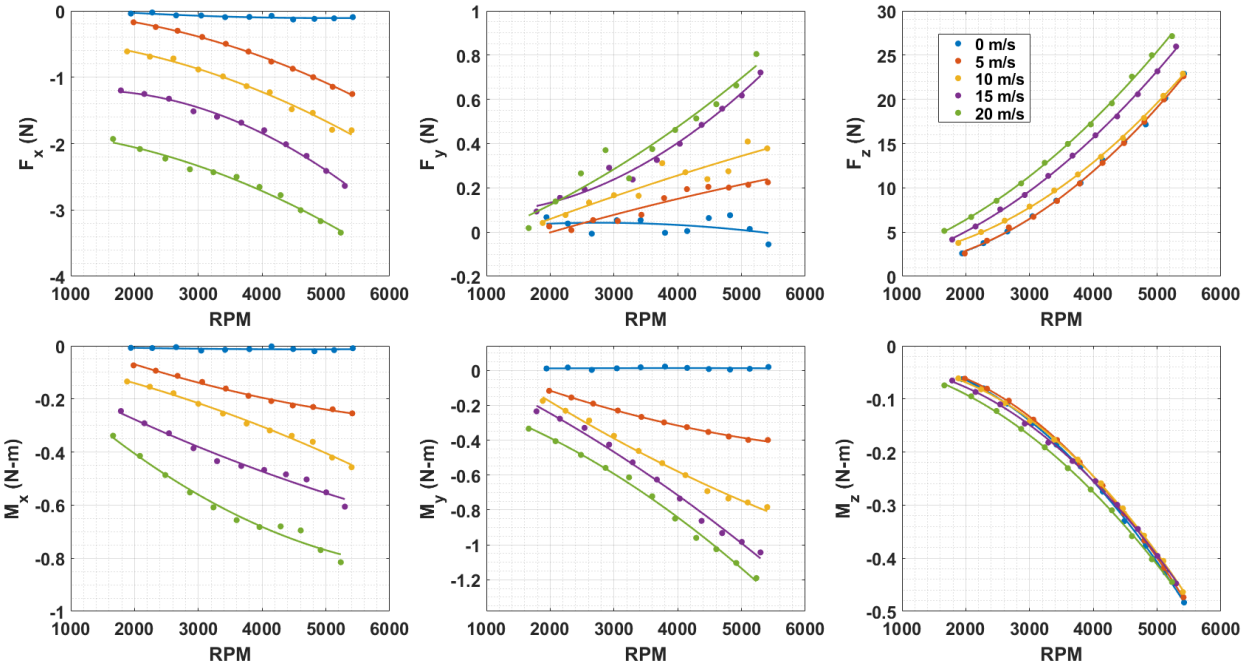


Figure A1 – Force and moments measured for 16x5.5 MR propeller as a function of RPM at different freestream velocities.

Table A3 – Quadratic polynomial fit coefficients for F_x, F_y, and F_z as functions of RPM.

Parameter	V_∞ [m/s]	p_1	p_2	p_3	RMSE	R^2
F_x	0	8.4800×10^{-9}	-8.5455×10^{-5}	0.1069	0.0171	0.7776
	5	-4.3646×10^{-8}	1.4550×10^{-6}	0.0009	0.0135	0.9990
	10	-4.6245×10^{-8}	-2.3825×10^{-5}	-0.3871	0.0518	0.9886
	15	-8.5903×10^{-8}	2.1500×10^{-4}	-1.3287	0.0437	0.9933
	20	-4.8633×10^{-8}	-3.7165×10^{-5}	-1.7881	0.0550	0.9880
F_y	0	-6.5581×10^{-9}	3.6321×10^{-5}	-0.0081	0.0417	0.1551
	5	-3.7169×10^{-9}	9.8145×10^{-5}	-0.1829	0.0261	0.9240
	10	-3.5221×10^{-9}	1.1964×10^{-4}	-0.1661	0.0459	0.8801
	15	2.9847×10^{-8}	-4.3719×10^{-5}	0.1008	0.0304	0.9822
	20	1.4893×10^{-8}	8.7091×10^{-5}	-0.1108	0.0629	0.9414
F_z	0	8.8812×10^{-7}	-8.0852×10^{-4}	0.9310	0.2274	0.9991
	5	8.9312×10^{-7}	-8.5849×10^{-4}	1.0439	0.1860	0.9994
	10	7.9368×10^{-7}	-4.3972×10^{-4}	1.9528	0.1481	0.9996
	15	7.3565×10^{-7}	8.9569×10^{-4}	0.3319	0.1762	0.9995
	20	7.1457×10^{-7}	1.3425×10^{-3}	0.8536	0.2293	0.9993

Table A4 – Quadratic polynomial fit coefficients for M_x, M_y, and M_z as functions of RPM.

Coefficient	V_∞ [m/s]	p_1	p_2	p_3	RMSE	R^2
M_x	0	7.6185×10^{-10}	-7.1878×10^{-6}	0.0039	0.0059	0.1306
	5	6.1158×10^{-9}	-9.9546×10^{-5}	0.1051	0.0051	0.9947
	10	-6.2754×10^{-9}	-4.3988×10^{-5}	-0.0274	0.0107	0.9920
	15	5.3179×10^{-9}	-1.2984×10^{-4}	-0.0387	0.0197	0.9744
	20	1.6726×10^{-8}	-2.3839×10^{-4}	0.0041	0.0241	0.9787
M_y	0	-4.1438×10^{-10}	3.2864×10^{-6}	0.0068	0.0069	0.0075
	5	1.0218×10^{-8}	-1.6121×10^{-4}	0.1654	0.0048	0.9981
	10	1.0890×10^{-8}	-2.6531×10^{-4}	0.3079	0.0204	0.9932
	15	-1.3504×10^{-8}	-1.5368×10^{-4}	0.1151	0.0300	0.9918
	20	-2.1713×10^{-8}	-9.7446×10^{-5}	-0.1052	0.0217	0.9956
M_z	0	-1.8796×10^{-8}	1.7200×10^{-5}	-0.0234	0.0026	0.9997
	5	-2.0418×10^{-8}	3.0298×10^{-5}	-0.0404	0.0014	0.9999
	10	-1.9055×10^{-8}	2.6093×10^{-5}	-0.0449	0.0025	0.9997
	15	-1.7278×10^{-8}	1.5339×10^{-5}	-0.0396	0.0038	0.9993
	20	-1.4846×10^{-8}	-3.0148×10^{-6}	-0.0259	0.0025	0.9997

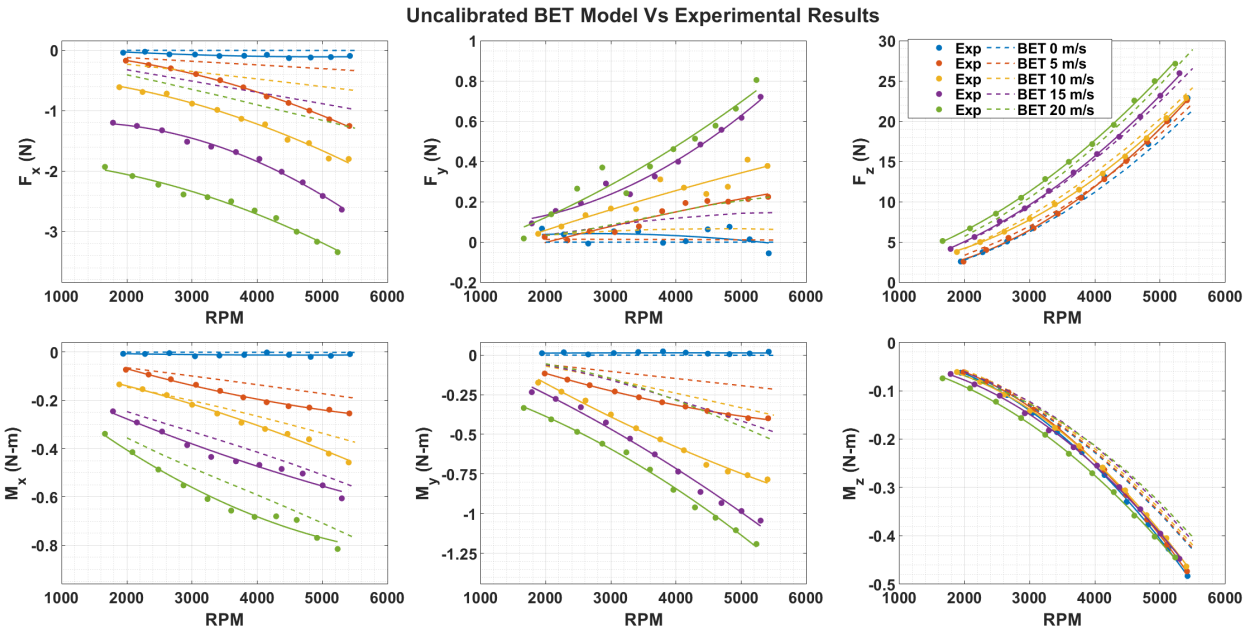


Figure A2 – Forces and moments obtained from the uncalibrated BET model compared against the experimental data.